

DIFFUSION MODELS ARE KELLY GAMBLERS

Akhil Premkumar

Department of Applied Physics
Yale University
New Haven, CT 06511, USA
akhil.prem@yale.edu

ABSTRACT

We draw a connection between diffusion models and the Kelly criterion for maximizing returns in betting games. We find that conditional diffusion models store additional information to bind the signal X with the conditioning information Y , equal to the mutual information between them. Classifier-free guidance effectively boosts the mutual information between X and Y at sampling time. This is especially helpful in image models, since the mutual information between images and their labels is low, a fact which is intimately connected to the manifold hypothesis. Finally, we point out some nuances in the popular perspective that diffusion models are infinitely deep autoencoders. In doing so, we relate the denoising loss to the Fermi Golden Rule from quantum mechanics.

1 INTRODUCTION

Diffusion models are highly effective at approximating continuous high-dimensional probability distributions like images, audio, and video (Sohl-Dickstein et al., 2015; Song et al., 2021b; Dhariwal & Nichol, 2021), and more recently, discrete data like language (Lou et al., 2024a; Nie et al., 2025). They generate samples by progressively denoising random vectors using information gathered during training—information that was eroded by the forward diffusion process as it transformed the data into noise. A method to estimate this information was introduced in Premkumar (2025).

The Kelly criterion is a rule for allocating capital in a betting game when you believe you have an information edge over the odds (Kelly, 1956). In particular, the financial value of side information is quantified by the mutual information between the game’s outcomes and the side information (Cover & Thomas, 2006). The mutual information between two random variables tells us how much knowing one variable reduces our uncertainty about the other, regardless of how complex their relationship is (Shannon, 1948). If the side information is a good indicator of the outcome, the mutual information between them is high, and so are our chances of winning.

In this work, we show that a diffusion model trained to generate X conditioned on Y stores additional information to associate X with Y . In an idealized limit, this is exactly the mutual information between X and Y (see Sec. 3). When the model generates a new sample of X given some side information $Y = y$, it is making a Kelly-style bet on the value of X . Just as in gambling, the bet is only good if $I(X; Y)$ is sufficiently large. Otherwise, the model tends to disregard the conditioning information. Classifier-free guidance (CFG) is a heuristic approach that addresses this issue by boosting the conditioning signal at sampling time (Ho & Salimans, 2022). In fact, CFG increases the mutual information between the condition and generated samples (see Sec. 4).

In image diffusion models, the difficulty in binding images with their labels stems from the low mutual information between the two. Most of an image’s information content resides in its fine perceptual details, which are largely shared between different image classes and therefore contribute little to distinguishing images with different macroscopic features. As the models resolve these small-scale details self-consistently, it is transporting a Gaussian ball from the ambient pixel space to a lower-dimensional manifold where the correlations between the pixels are very tight. Locating such a manifold requires a substantial reduction in uncertainty, which is why the perceptual components dominate the information budget. The price of determinism is information.

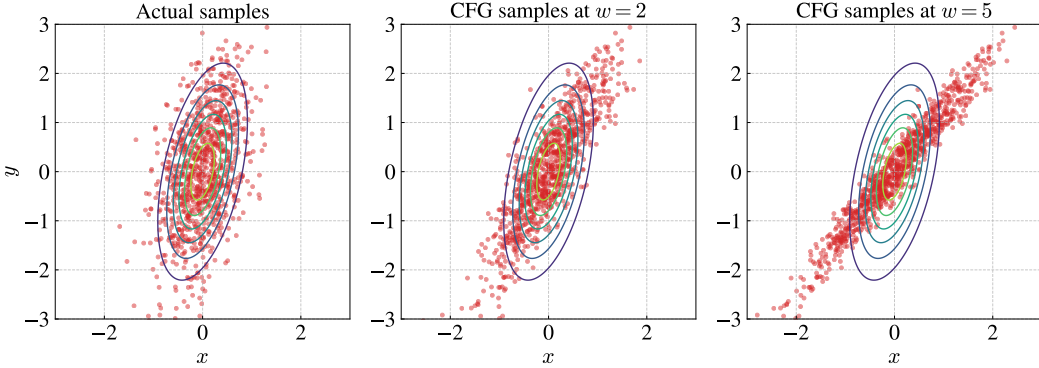


Figure 1: Samples generated by a CFG-style modification to the conditional score $\nabla \log p(x_t, t|y)$ of a joint Gaussian (cf. Eqs. (16) and (26)). CFG strengthens the correlation between X and Y , increasing their mutual information. But it also alters the relationship between them. The central theme of this paper is to study diffusion models through the lens of mutual information.

2 KELLY CRITERION

We begin with a brief discussion of Kelly’s argument using a toy example. Simplifying assumptions are made to emphasize ideas central to the rest of the paper. For a more rigorous treatment, see Kelly (1956), Chapter 4 of Cover & Thomas (2006) or Thorp (2011).

Consider a simple betting game involving a cup that conceals a six-sided die. A dealer rattles the die with a firm shake of the cup and invites us to place bets on the outcome. Believing that the die is fair, the dealer offers 6-for-1 odds—if we bet \$1 on a number and win, we receive \$6, and nothing otherwise. Let the random variable X represent the outcome of a single roll. Over n i.i.d. throws, the outcome $\mathbf{x} = (x_1, x_2, \dots, x_n)$ is almost certain to belong to the typical set of $2^{nH(X)}$ members, each having nearly the same probability when n is large. This is the asymptotic equipartition principle (see Ch. 4 of MacKay (2002)). Here $H(X) := \mathbb{E}[-\log_2 p(x)]$ is the Shannon entropy of X . To optimize our gains we can distribute our seed money V_0 equally over the typical set and let the game run.¹ The winning sequence will return 6^n times the investment placed on it, so we make a total of $V_n = 2^{n(\log_2 6 - H(X))} V_0$ by the end. We profit because the dealer assumed the die was fair, hence the 6-for-1 odds, while we placed our bets according to the true distribution of outcomes, which is the *Kelly criterion*.

Now suppose that, unbeknownst to the dealer, there is a communication channel that transmits the outcome to us before the cup is lifted. If the channel is noiseless, we are guaranteed to win every round, and we can grow our wealth by a factor of 6^n over n throws by wagering our entire stake on the correct outcome each time. In other words, a perfect channel eliminates all uncertainty about the outcome, which is equivalent to setting $H(X) \rightarrow 0$ in the previous analysis.

On the other hand, if the channel is noisy, we can no longer be certain that the information we receive accurately reflects the outcome under the cup; the noise in the channel reintroduces randomness into the game. However, the side information may be correlated with the outcome if the noise is not too severe, so we can do better than when we did not know the outcome at all. If Y is the signal received from the channel, we can place bets according to $p(x|y)$ rather than $p(x)$. That is, we repeat the arguments from above with $H(X)$ replaced by the conditional entropy $H(X|Y)$, which quantifies the residual uncertainty about X given access to Y —knowing Y allows us to concentrate our bets on just $2^{nH(X|Y)}$ sequences. Then, optimal betting yields a final wealth of $V'_n = 2^{n(\log_2 6 - H(X|Y))} V_0$. Thus, the increase in doubling rate *due to the communication channel* is the mutual information between X and Y (see Sec. A.1),

$$R := \lim_{n \rightarrow 0} \frac{1}{n} \log_2 \frac{V'_n}{V_n} = H(X) - H(X|Y) \equiv I(X; Y). \quad (1)$$

¹This is equivalent to placing bets sequentially after each outcome is revealed; see Example 6.3.1 in Cover & Thomas (2006).

3 THE DIFFUSION GAMBLER

Given a set of data vectors $\{\mathbf{x}^{(i)}\}_{i=1}^N$ in \mathbb{R}^{D_X} , a probabilistic model approximates the underlying distribution p_d from which these vectors could have been sampled. One way to do this is to transform a generic initial distribution p_0 into one that is more likely to have produced the given samples. If p_0 is nearly the equilibrium state of a diffusive process (see Sec. F for notation)

$$d\tilde{\mathbf{X}}_s = b_+(\tilde{\mathbf{X}}_s, s)ds + \sigma(s)d\hat{\mathbf{B}}_s, \quad (2)$$

then the transformation we seek is simply a reversal (playback) of the forward evolution that converts $p_d \rightarrow p_0$ according to Eq. (2). The reverse process is effected by

$$d\mathbf{X}_t = -(b_+(\mathbf{X}_t, T-t) - \sigma(T-t)^2 \nabla \log p(\mathbf{X}_t, t))dt + \sigma(T-t)d\mathbf{B}_t, \quad (3)$$

where $t := T - s$ is a time variable that runs in the opposite direction to s , and p is the density that interpolates p_0 and p_d (see Fig. 11). Diffusion is a dissipative process that erases information over time, which means reversal must reinstate the same amount of information to drive p_0 back to p_d . If p_d is subject to Eq. (2) for a time T , and b_+, σ have the same time-dependence, the information that must be injected to return to p_d is quantified by the total entropy produced (Vaikuntanathan & Jarzynski, 2009; Seifert, 2012),

$$S_{\text{tot}} := \int_0^T dt \frac{\sigma^2}{2} \mathbb{E}_p \left[\left\| \nabla \log p_{\text{eq}}^{(t)} - \nabla \log p \right\|^2 \right] = D_{\text{KL}} \left(p_d \| p_{\text{eq}}^{(T)} \right) - D_{\text{KL}} \left(p_0 \| p_{\text{eq}}^{(0)} \right). \quad (4)$$

The expectation is taken over trajectories generated by Eq. (2), starting at $\tilde{\mathbf{X}}_0 \sim p_d$, and $p_{\text{eq}}^{(t)}$ is the quasi-invariant state, which can be understood as the ‘least informative state’ at time t . It is the distribution that would result if we froze b_+ and σ at their values at t and waited for the system to equilibrate. That is, $p_{\text{eq}}^{(t)}(x) \propto \exp \left[\int^x 2b_+/\sigma^2 \right]$. In a diffusion model the drift term in Eq. (3) is approximated by a neural network. It is useful to parameterize the reverse SDE as

$$d\mathbf{X}_t = (b_+(\mathbf{X}_t, T-t) + \sigma(T-t)^2 e_{\theta}(\mathbf{X}_t, T-t))dt + \sigma(T-t)d\mathbf{B}_t, \quad (5)$$

where the neural network e_{θ} is trained to minimize (cf. Sec. B.3)

$$\mathcal{L} = \int_0^T dt \frac{\sigma^2}{2} \mathbb{E}_p \left[\left\| \nabla \log p_{\text{eq}}^{(t)} - \nabla \log p + e_{\theta} \right\|^2 \right]. \quad (6)$$

If $e_{\theta} = 0$, Eq. (5) reduces to the forward dynamics, Eq. (2). Then, the probability that N random vectors from p_0 would be distributed as p_d at $t = T$ is $\simeq \exp(-NS_{\text{tot}})$ (Chetrite et al., 2021). A *perfectly* trained diffusion model, with the idealized network $e_{\theta}^* = -2b_+/\sigma^2 + \nabla \log p$, modifies the dynamics to Eq. (3), which is guaranteed to take $p_0 \rightarrow p_d$. Such a network stores precisely S_{tot} worth of information, which is why they are called *entropy-matching* models (Premkumar, 2025).

Information negates uncertainty. The idealized entropy-matching model applies S_{tot} worth of information to reconstitute p_d from p_0 in time T . If T is large enough that $p_0 \approx p_{\text{eq}}^{(0)}$, the total entropy can be written as

$$S_{\text{tot}}^{\mathbf{X}} = D_{\text{KL}} \left(p_d(\mathbf{x}) \| p_{\text{eq}}^{(T)}(\mathbf{x}) \right) = -S(\mathbf{X}) - \int d\mathbf{x} p_d(\mathbf{x}) \log p_{\text{eq}}^{(T)}(\mathbf{x}). \quad (7)$$

We have introduced a superscript \mathbf{X} in $S_{\text{tot}}^{\mathbf{X}}$ to specify explicitly the random variable whose distribution is being modeled. Next, we consider a scenario where the diffusion model is used for conditional generation. Let \mathbf{Y} be the conditioning information. For example, \mathbf{Y} represents the class labels in class-conditioned image generation, with \mathbf{X} being the associated images. Given $\mathbf{Y} = \mathbf{y}$, a new sample can be generated by applying Eq. (5) with

$$e_{\theta}^*(\mathbf{x}_t, T-t; \mathbf{y}) = -\frac{2b_+(\mathbf{x}_t, T-t)}{\sigma^2(T-t)} + \nabla \log p(\mathbf{x}_t, t|\mathbf{y}). \quad (8)$$

Let $S_{\text{tot}}^{\mathbf{X}|\mathbf{y}}$ denote the information stored by such a network for each \mathbf{y} . On average, this model injects an amount of information

$$S_{\text{tot}}^{\mathbf{X}|\mathbf{Y}} := \mathbb{E}_{\mathbf{Y}} \left[S_{\text{tot}}^{\mathbf{X}|\mathbf{y}} \right] = \mathbb{E}_{\mathbf{Y}} \left[D_{\text{KL}} \left(p_d(\mathbf{x}|\mathbf{y}) \| p_{\text{eq}}^{(T)}(\mathbf{x}) \right) \right] = -S(\mathbf{X}|\mathbf{Y}) - \int d\mathbf{x} p_d(\mathbf{x}) \log p_{\text{eq}}^{(T)}(\mathbf{x}). \quad (9)$$

Notice that the conditional model injects an *additional* R nats of information, where

$$R := S_{\text{tot}}^{\mathbf{X}|\mathbf{Y}} - S_{\text{tot}}^{\mathbf{X}} = S(\mathbf{X}) - S(\mathbf{X}|\mathbf{Y}) \equiv I(\mathbf{X}; \mathbf{Y}). \quad (10)$$

Thus, the generative step is a *Kelly bet on the value of \mathbf{X} using the side information \mathbf{Y}* . More importantly, $S_{\text{tot}}^{\mathbf{X}|\mathbf{Y}} \geq S_{\text{tot}}^{\mathbf{X}}$, since additional information is needed to squeeze the quasi-invariant state into the distributions $p_{\text{d}}(\mathbf{x}|\mathbf{y})$, which are on average narrower than the marginal $p_{\text{d}}(\mathbf{x})$ (see Sec. A.1). At first, this may seem like a peculiar feature of information storage in diffusion models—usually, knowing side information \mathbf{Y} lets us build a shorter conditional code for $\mathbf{X}|\mathbf{Y}$, saving us $I(\mathbf{X}; \mathbf{Y})$ bits of storage (Slepian & Wolf, 1973). Diffusion models do the opposite: they store *more* information when some knowledge about \mathbf{X} is already available through \mathbf{Y} . Conversely, the model retains less information when nothing is known about \mathbf{X} .

The apparent discrepancy is resolved by noting that storing shorter codes for $\mathbf{X}|\mathbf{Y}$ incurs an additional compute cost during recall. For example, if \mathbf{Y} is one half of the image \mathbf{X} , then we need to store only the other half of the image in a conventional memory. However, given some \mathbf{y} , we must *search* for the matching halves that are consistent with \mathbf{y} to reconstitute the full \mathbf{x} . On the other hand, a diffusion model trained on pairs of half-images and full images stores additional information to directly associate the two. Thus, the diffusion model trades off memory for compute at the generative stage, which is a form of amortized inference (Xu et al., 2020).

Entropy-matching In the discussion above we have parameterized the reverse drift in Eq. (5) as $b_+ + \sigma^2 \mathbf{e}_\theta$, which is different from the score-matching parameterization of $-b_+ + \sigma^2 \mathbf{s}_\theta$. The latter forces the network to retain additional information to counteract the repulsive $-b_+$ term, as explained in Premkumar (2025). A simple thought experiment reveals the problem: suppose we take $p_{\text{d}} = p_0 \approx p_{\text{eq}}^{(0)}$. The forward process has little effect on the distribution since p_{d} is already close to equilibrium. However, the scores for this transformation are still non-zero over the support of $p_{\text{eq}}^{(0)}$, which means the network in a score-matching model must retain information to convert a distribution *back to itself*. On the other hand, an entropy-matching network would store no information in this scenario, as expected. In this sense, entropy-matching makes transparent the correspondence between the network’s information content and the entropy of the underlying data.

Entropy-matching also reveals an interesting fact about correlations within the components of \mathbf{X} . In the unconditional case, with T large enough that $p_0 \approx p_{\text{eq}}^{(0)}$, the total entropy can be factorized as

$$S_{\text{tot}} = D_{\text{KL}} \left(p_{\text{d}} \parallel p_{\text{eq}}^{(T)} \right) = \sum_{k=1}^{D_{\mathbf{X}}} D_{\text{KL}} \left(p_{\text{d}}(x_k) \parallel p_{\text{eq}}^{(T)}(x_k) \right) + \underbrace{D_{\text{KL}} \left(p_{\text{d}}(x_1, \dots, x_{D_{\mathbf{X}}}) \parallel \prod_{k=1}^{D_{\mathbf{X}}} p_{\text{d}}(x_k) \right)}_{\text{TC}(\mathbf{X})}. \quad (11)$$

The last term, called the *total correlation*, is a generalization of mutual information to multiple random variables (Watanabe, 1960). In Eq. (11) x_k is the k -th component of a data vector \mathbf{x} , and $p_{\text{d}}(x_k)$ and $p_{\text{eq}}^{(T)}(x_k)$ are the marginal densities obtained by integrating $p_{\text{d}}(\mathbf{x})$ and $p_{\text{eq}}^{(T)}(\mathbf{x})$ over all components except x_k . Eq. (11) tells us that during the reversal/generative stage, the model must (1) shift the marginals for each x_k from $p_{\text{eq}}^{(T)}(x_k) \rightarrow p_{\text{d}}(x_k)$, and (2) establish correlations between different x_k . Thus, denoising a vector from p_0 is, in part, the process of *restoring the component-wise correlations* that were lost in the forward stage.

Neural Entropy We derived Eq. (10) under the assumption of an ideal entropy-matching model \mathbf{e}_θ^* , which absorbs exactly S_{tot} units of information during training. In practice, no model achieves this ideal because of the finite number of training epochs, limited batch size, and finite data. However, Premkumar (2025) demonstrates that the amount of information stored in a real network \mathbf{e}_θ is measured through its *neural entropy*,

$$S_{\text{NN}}^{\mathbf{X}} := \int_0^T ds \frac{\sigma(s)^2}{2} \mathbb{E}_p \left[\|\mathbf{e}_\theta(\tilde{\mathbf{x}}_s, s)\|^2 \right]. \quad (12)$$

Notice that setting $\mathbf{e}_\theta \rightarrow \mathbf{e}_\theta^*$ turns $S_{\text{NN}} \rightarrow S_{\text{tot}}$, which follows from Eqs. (4) and (6). Away from this theoretical limit the neural entropy can be either smaller or larger than the true S_{tot} . For example, when the dataset is sparse the diffusion model tends to concentrate probability mass around

the available samples, demanding greater effort from the network than it requires to reconstitute the true p_d , which may have a more distributed support. Another possibility is that training is not long enough for the network to absorb all of S_{tot} , so neural entropy trails the true value. Nevertheless, with sufficient training and a large enough dataset, Eq. (12) provides a close approximation to S_{tot} (see Fig. 5). These are the entropy-matching models we discuss henceforth.

4 MUTUAL INFORMATION AND GUIDANCE

It is possible to use Eq. (10) to estimate the mutual information between two high-dimensional random variables. Given a set of pairs $\{(\mathbf{x}^{(i)}, \mathbf{y}^{(i)})\}_{i=1}^N$ we can train an entropy-matching model to reconstruct the distribution of \mathbf{X} given \mathbf{Y} and, separately,² the marginal distribution of \mathbf{X} . The difference in neural entropy between the two approximates $I(\mathbf{X}; \mathbf{Y})$. This approach is closely related to the results in Franzese et al. (2024). Specifically, their Eq. (19) says

$$I(\mathbf{X}; \mathbf{Y}) = \mathbb{E}_{\mathbf{Y}} \left[\int_0^T ds \frac{\sigma^2}{2} \mathbb{E}_{\tilde{\mathbf{X}}_s, \mathbf{X} | \mathbf{y}} \left[\|\nabla \log p(\tilde{\mathbf{x}}_s, s | \mathbf{y}) - \nabla \log p(\tilde{\mathbf{x}}_s, s)\|^2 \right] \right] \quad (13)$$

$$\approx \mathbb{E}_{\mathbf{Y}} \left[\int_0^T ds \frac{\sigma^2}{2} \mathbb{E}_{\tilde{\mathbf{X}}_s, \mathbf{X} | \mathbf{y}} \left[\|e_{\theta}(\tilde{\mathbf{x}}_s, s; \mathbf{y}) - e_{\theta}(\tilde{\mathbf{x}}_s, s)\|^2 \right] \right], \quad (14)$$

up to terms that vanish as $T \rightarrow 0$. We give an alternative derivation of this result in Sec. C.1. Notice that Eq. (14) also works with score-matching models, with e_{θ} replaced by the corresponding s_{θ} . The main advantage of entropy-matching is that it links the information stored in the network to the effort required to reconstitute p_d . For now, we consider how Eq. (13) helps us better understand classifier-free guidance (CFG) (Ho & Salimans, 2022).

In image models, \mathbf{X} denotes images and \mathbf{Y} the corresponding class labels. Dhariwal & Nichol (2021) show that the quality of generated samples can be improved, at the cost of decreased diversity, by forcing the model to adhere more strongly to the conditioning variable. If Eq. (3) evolves p_0 to $p(\mathbf{x}_t, t | \mathbf{y})$ at time t , the conditioning on \mathbf{y} can be amplified by modifying the drift vectors to sample from $p(\mathbf{x}_t, t | \mathbf{y})p(\mathbf{y} | \mathbf{x}_t, t)^w$ instead, where $w > 0$ is a parameter we can control. Ho & Salimans (2022) accomplish this by constructing an implicit classifier $p(\mathbf{y} | \mathbf{x}_t, t) \propto p(\mathbf{x}_t, t | \mathbf{y})/p(\mathbf{x}_t, t)$, which has the score

$$\begin{aligned} s_{\text{cl}}(\mathbf{y}, t) &:= \nabla_{\mathbf{x}_t} \log p(\mathbf{y} | \mathbf{x}_t, t) = \nabla_{\mathbf{x}_t} \log p(\mathbf{x}_t, t | \mathbf{y}) - \nabla_{\mathbf{x}_t} \log p(\mathbf{x}_t, t) \\ &\equiv \nabla_{\tilde{\mathbf{x}}_s} \log p(\tilde{\mathbf{x}}_s, s | \mathbf{y}) - \nabla_{\tilde{\mathbf{x}}_s} \log p(\tilde{\mathbf{x}}_s, s) \approx e_{\theta}(\tilde{\mathbf{x}}_s, s; \mathbf{y}) - e_{\theta}(\tilde{\mathbf{x}}_s, s). \end{aligned} \quad (15)$$

This is also the vector whose ℓ_2 -norm appears in Eq. (13). A close examination of the latter helps us build some intuition for s_{cl} . We begin by noting that the inner expectation in Eq. (13) is computed over trajectories that start from samples of $\mathbf{X} | \mathbf{Y} = \mathbf{y}$ (or $\mathbf{X} | \mathbf{y}$ for short). If we were to average $\|s_{\text{cl}}(\mathbf{y}, s)\|^2$ over forward paths that emanate from $\mathbf{X} | \mathbf{y}'$ where $\mathbf{y}' \neq \mathbf{y}$, the expectation value would be higher, since the conditional score $\nabla \log p(\tilde{\mathbf{x}}_s, s | \mathbf{y})$ along those paths are larger. That is, the conditional scores are steeper in regions explored by diffused versions of $\mathbf{X} | \mathbf{y}'$, where the underlying conditional density $p(\tilde{\mathbf{x}}_s, s | \mathbf{y})$ falls off rapidly. Therefore, the integral over $\mathbb{E}_{\tilde{\mathbf{X}}_s, \mathbf{X} | \mathbf{y}'} \|s_{\text{cl}}(\mathbf{y}, s)\|^2$ is *smallest* when $\mathbf{y}' = \mathbf{y}$.³ During the generative process, a sample can be made more \mathbf{y} -like by augmenting the reverse drift term in Eq. (3) with $w \times s_{\text{cl}}(\mathbf{y}, t)$:

$$\nabla \log p(\mathbf{x}_t, t | \mathbf{y}) \rightarrow (1 + w) \nabla \log p(\mathbf{x}_t, t | \mathbf{y}) - w \nabla_{\mathbf{x}_t} \log p(\mathbf{x}_t, t). \quad (16)$$

This is CFG. The new drift term pulls a reverse-evolving \mathbf{x}_t more strongly toward regions in \mathbf{x} -space that are consistent with the condition \mathbf{y} . At the next time step, $\mathbf{x}_{t+\Delta t}$ is more \mathbf{y} -like, so $s_{\text{cl}}(\mathbf{y}, t)$ *weakens*. Therefore, the effect of CFG diminishes over time t . In the limit, the fully denoised sample will be more tightly determined by \mathbf{y} , so $I(\mathbf{X}; \mathbf{Y})_{\text{CFG}}$ will be higher (see Fig. 4).

One might wonder whether it is possible to substitute Eq. (16) into Eq. (13) to conclude that mutual information is boosted to $(1 + w)^2 I(\mathbf{X}; \mathbf{Y})$. But that would be incorrect; such a maneuver is

²In practice, the same network can parameterize both the conditional and unconditional drifts. For example, in class-conditioned image models, class labels are randomly dropped during training and replaced with a learned null embedding, allowing the model to learn the unconditional drift (Ho & Salimans, 2022).

³In fact, it is possible to build a classifier based on this very insight (Clark & Jaini, 2023; Li et al., 2023).

disallowed by the fact that the modified score does not correspond to any known forward diffusion process. For the same reason, the distribution we reconstruct under CFG is not the true p_d (see Fig. 1). We discuss this point further in Sec. C.2. It remains true, however, that CFG strengthens the binding between \mathbf{X} and \mathbf{Y} . This is especially useful when the base training cannot reliably ensure that conditioning is respected. The underlying reason for this is often the training data itself, and not the model.

Mutual information is largest if knowledge of the value of one variable completely determines the value of the other (see Sec. A.1). On the other hand, if a given value of \mathbf{Y} corresponds to a wide range of \mathbf{X} , a greater amount of uncertainty remains about the value of the latter, so $I(\mathbf{X}; \mathbf{Y})$ is low. This is the case with labeled image datasets, where a label $\mathbf{Y} = \mathbf{y}$ can correspond to a rich distribution of images $\mathbf{X}|\mathbf{Y} = \mathbf{y}$. For instance, the label ‘dog’ corresponds to a wide variety of dogs. There is, however, a subtle point here about image datasets: the entropy of images does not arise only from high-level semantic variation (different breeds, poses, or scenes), but is overwhelmingly dominated by the low-level perceptual details present in each image. Diffusion models capture these details with remarkable fidelity, and a large share of their information capacity is devoted to encoding fine perceptual structure rather than high-level semantics. In fact, much of the low-level detail is not class-specific, but is shared across multiple categories of images (see Fig. 9). Therefore, specifying the label ‘dog’ does very little to narrow down the possibilities of which sample to draw. This is why diffusion models often stray from the conditioning signal during generation: the mutual information between images and labels is intrinsically low.

Perceptual details overwhelm the information budget due to a pathological property of mutual information between continuous random variables. Unlike the discrete case, $I(X; Y)$ between two perfectly correlated continuous random variables X and Y is infinite—specifying a real number requires infinitely many digits, so we gain an infinite amount of information about X from a given $Y = y$. More formally, the joint density $p(x, y)$ collapses to a lower-dimensional manifold, since $Y = f(X)$, whereas the product density $p(x)p(y)$ is supported over the full joint space. The KL between them, namely $I(X; Y)$, therefore diverges (see Sec. A.1). In case of diffusion models, the correlation between pixels must be made rigid to pin down the small-scale details, which causes a similar divergence in the $\text{TC}(\mathbf{X})$ term in Eq. (11), as the components x_k converge to a lower-dimensional surface in pixel space (see Fig. 8). We provide empirical proof of these statements in Sec. E, where we probe the information captured by the network at different length scales using a diffusion autoencoder.

5 DIFFUSION AUTOENCODERS

A diffusion model can develop its own side information when it is paired with an encoder. This arrangement is called a *diffusion autoencoder*, or DAE (Preechakul et al., 2022). Recall that a standard variational autoencoder (VAE) is trained to minimize the negative of the evidence lower bound (Kingma & Welling, 2014),

$$-\text{ELBO}(\mathbf{x}) = \mathbb{E}_{q_\phi(\mathbf{z}|\mathbf{x})}[-\log p_\theta(\mathbf{x}|\mathbf{z})] + \gamma D_{\text{KL}}(q_\phi(\mathbf{z}|\mathbf{x}) \parallel p(\mathbf{z})) \quad (17)$$

where ϕ and θ are the encoder and decoder parameters respectively. The coefficient γ plays the role of the weighting factor in the β -VAE objective (Higgins et al., 2017), balancing reconstruction and KL terms. In a DAE, the reconstruction term is replaced by the upper bound

$$\begin{aligned} \mathbb{E}_{\mathbf{X}, \mathbf{Z}}[-\log p_\theta(\mathbf{x}|\mathbf{z})] + c \leq \\ \int_0^T ds \mathbb{E}_{\mathbf{X}, \mathbf{Z}, \tilde{\mathbf{X}}_s} \left[\frac{\sigma^2}{2} \left\| \nabla \log p_{\text{eq}}^{(s)}(\tilde{\mathbf{x}}_s) - \nabla \log p(\tilde{\mathbf{x}}_s, s|\mathbf{x}, 0) + \mathbf{e}_\theta(\tilde{\mathbf{x}}_s, s; \mathbf{z}) \right\|^2 \right] =: \mathcal{L}_{\text{DEM}}^{\mathbf{X}|\mathbf{Z}}. \end{aligned} \quad (18)$$

Here c is a constant with respect to the network parameters θ (cf. Eq. (37)). The expectation over \mathbf{X} and $\tilde{\mathbf{X}}_s$ averages over the data points $\{\mathbf{x}^{(i)}\}_{i=1}^N$ and their value at time s under the forward process in Eq. (2). Importantly, the bound is precisely the denoising entropy-matching objective used to train the diffusion model; minimizing this loss is equivalent to maximizing log likelihood (see Sec. B.1). A score-matching parameterization can also be used in Eq. (18). The latents \mathbf{z} are sampled from the encoder,

$$q_\phi(\mathbf{z}|\mathbf{x}) = \mathcal{N}(\mathbf{z}; \mu_\phi(\mathbf{x}), \text{diag}(\sigma_\phi^2(\mathbf{x}))), \quad (19)$$

using the reparameterization trick to enable gradient-based training. Conditioning on \mathbf{z} allows the diffusion model to concentrate the probability mass to a smaller region in \mathbf{x} -space compared to

the unconditional case; on average, conditional distributions are narrower than the marginals (cf. Eq. (10)). If the diffusion model had perfect freedom to choose the latent it would assign a unique $z^{(i)}$ to each $x^{(i)}$ in the dataset, since that would lead to maximal concentration of probability in each conditional distribution. However, the DAE is unable to do so because (i) the inductive biases of the diffusion model temper its ability to perfectly resolve each $x^{(i)}$, which is good because it avoids overfitting (Kadkhodaie et al., 2023), and (ii) the encoder admits a narrow range of z , so the diffusion decoder has a limited set of latent codes to choose from—the DAE is an *information bottleneck* (see Sec. A.2). Therefore, jointly minimizing the encoder term with the upper bound from Eq. (18) forces the diffusion model to negotiate a latent Z that is maximally correlated with X , under the given constraints. This follows from

$$\max I(X; Z) \equiv S(X) - \min S(X|Z) \equiv S(X) - \min \mathbb{E}_{X,Z}[-\log p_\theta(x|z)], \quad (20)$$

since the cross entropy $\mathbb{E}_{X,Z}[-\log p_\theta(x|z)]$ upper bounds the conditional entropy $S(X|Z)$, and $S(X) := \mathbb{E}_X[-\log p_d(x)]$ is independent of θ or ϕ . The latent Z is a compressed proxy for how the diffusion model represents X . We use this fact in Sec. E, where the hierarchical nature of the information stored in these models is revealed through the structure they induce on the latents.

Minimizing Eq. (18) implicitly *maximizes* $S_{NN}^{X|Z}$, as evident from Eqs. (9) and (20)—a strongly correlated latent forces the diffusion model to discern tighter (on average) distributions of $X|Z$, which requires a higher neural entropy, whereas a weak latent does the opposite. This makes the DAE a great conceptual tool to understand how conditioning affects retention. Consider first the limiting case where the encoder is just the identity operator, so $Z = X$. There is now a unique $z^{(i)}$ for each $x^{(i)}$, so every $p_\theta(x|z)$ is a delta function, and the neural entropy $S_{NN}^{X|Z}$ is very large—the diffusion model has *memorized* each $x^{(i)}$. At the other extreme, we can imagine an encoder that maps every value of $x^{(i)}$ to a single value, call it z_{null} . This converts the decoder into an unconditional diffusion model since it receives no information about X from the encoder. Consequently, the model learns to reconstruct the broadest possible distribution of X , and $S_{NN}^{X|Z}$ reaches its lowest possible value, S_{NN}^X . So the model retains the smallest amount of information when it is least committed to recovering each $x^{(i)}$ perfectly.

This argument also connects to the tension between conditioning and generalization. In Sec. 4 we discussed the weak correlation between images X and their labels Y . If $I(X; Y)$ was stronger it would reduce the diversity in samples produced because the model has memorized more information. The power of CFG is that it is applied during the generative stage, so the model does not have to overcommit to the given data during training. However, CFG does have a fundamental limitation: if the underlying dependence between X and Y is weak, amplification of the signal can only go so far. DAE’s allow an alternative approach: a second diffusion model is trained to generate from Y the latent Z first, which is then used to produce X . The latent Z abstracts away the perceptual details that overwhelm the correlation between X and Y , while also being expressive enough to encode the variation in the semantic structure of X .

6 THE INFINITE TOWER

Our discussion so far has revolved around coarse information-theoretic quantities such as entropy and mutual information. We will now develop a geometric view of diffusion models, with particular attention to how they resolve the nuanced structure of complex distributions in small, continuous increments. For clarity, we focus on unconditional diffusion models for the moment. We begin by noting that the bound in Eq. (18) is saturated iff $\nabla \log p_{\text{eq}} + e_\theta = \nabla \log p$, with $p_\theta = p_d$ (cf. Eq. (45)),

$$\mathbb{E}_X[-\log p_d(x)] + c = \int_0^T ds \frac{\sigma^2}{2} \mathbb{E}_{X, \tilde{X}_s} \left[\|\nabla_{\tilde{x}_s} \log p(\tilde{x}_s, s) - \nabla \log p(\tilde{x}_s, s|x, 0)\|^2 \right]. \quad (21)$$

We also assume that the forward noising process has a Gaussian transition kernel, which holds when the drift is either zero or affine (e.g. the VE and VP processes from Song et al. (2021b)). For such processes, the score function is given by the Miyasawa relation, Eq. (44). In simple terms, this relation states that at any given s , the ideal score is a vector pointing from \tilde{x}_s toward the denoised mean $\hat{x}(\tilde{x}_s) := \mathbb{E}[x|\tilde{x}_s]$, scaled by a forward factor. Then, Eq. (45) takes the form (cf. Eq. (46))

$$\mathbb{E}_X[-\log p_d(x)] + c = \int_0^T ds B(s) \mathbb{E}_{X, \tilde{X}_s} \left[\|\hat{x}(\tilde{x}_s) - x\|^2 \right]. \quad (22)$$

Intuitively, $\hat{\mathbf{x}}(\tilde{\mathbf{x}}_s)$ is the average over all samples from p_d that had a *reasonable* probability of landing at $\tilde{\mathbf{x}}_s$ at time s under the forward SDE, Eq. (2). Each point in p_d can only travel so far under this process, so $\hat{\mathbf{x}}(\tilde{\mathbf{x}}_s)$ is the mean of points in p_d that are closest to $\tilde{\mathbf{x}}_s$, since those are the points that are most likely to arrive at $\tilde{\mathbf{x}}_s$ in finite time. Given $\tilde{\mathbf{x}}_s$, we can imagine firing off a swarm of stochastic trajectories from $\tilde{\mathbf{x}}_s$ back to $s = 0$, each of them evolving according to the reverse SDE, Eq. (3). The mean of the distribution of their endpoints is $\hat{\mathbf{x}}(\tilde{\mathbf{x}}_s)$.

We can sharpen our intuition further by examining Eq. (22) for a single test point \mathbf{x} . That is, we lift the expectation over $\tilde{\mathbf{X}}$ to obtain

$$-\log p_d(\mathbf{x}) + c'(\mathbf{x}) = \int_0^T ds B(s) \mathbb{E}_{\tilde{\mathbf{X}}_s} \left[\|\hat{\mathbf{x}}(\tilde{\mathbf{x}}_s) - \mathbf{x}\|^2 \mid \tilde{\mathbf{X}}_0 = \mathbf{x} \right]. \quad (23)$$

Here c' is related to c as $c = \mathbb{E}_{\tilde{\mathbf{X}}} [c'(\mathbf{x})]$. Operationally, the r.h.s. can be evaluated through the following procedure: starting at \mathbf{x} , release a set of trajectories that follow the forward process, Eq. (2), and sample them at s to get a collection of $\tilde{\mathbf{x}}_s$ (see Fig. 12a). For each such $\tilde{\mathbf{x}}_s$, compute $\hat{\mathbf{x}}(\tilde{\mathbf{x}}_s)$, the mean of points in p_d that could have produced $\tilde{\mathbf{x}}_s$ under the forward process (see Figs. 12b and 12c). Therefore, the expectation over $\tilde{\mathbf{X}}_s$ is an average over the ℓ_2 -distance from the point \mathbf{x} to all candidates from p_d that are most similar to \mathbf{x} .

Propagating to $\tilde{\mathbf{x}}_s$ and traveling back to $\hat{\mathbf{x}}$ is how we locate candidates most like \mathbf{x} . The average in Eq. (23) admits a broader range of such options if s is larger. This is because the $\tilde{\mathbf{x}}_s$ samples at late s have little memory of where they started, so they could have come from almost anywhere in p_d as well. In other words, the integrand ‘sees more’ of p_d at larger s . In the very late time limit $\mathbb{E}[\mathbf{x}|\tilde{\mathbf{x}}_s] \approx \mathbb{E}[\mathbf{x}]$, the mean of p_d . Conversely, at smaller values of s we resolve the mean of a narrower range of the most \mathbf{x} -like points from p_d . Thus, Eq. (23) compares the test point with denoised means that become increasingly more specific as $s \rightarrow 0$ (see Fig. 13). Such gradual refinement echoes the logic of Huffman coding, in which symbols are distinguished by progressively finer splits (Huffman, 1952).

Connection to Quantum Mechanics At this point, readers with a physics background may notice an analogy to the *Fermi Golden Rule* for the transition rates between quantum states (Sakurai & Napolitano, 2020). With a mild abuse of the Dirac notation, the picture above can be formalized as

$$-\log p_d(\mathbf{x}) + c'(\mathbf{x}) = \int_0^T ds B(s) \int d\tilde{\mathbf{x}}_s \int d\mathbf{x}' \langle \mathbf{x}' \mid \mathfrak{D}_s^\dagger \mid \tilde{\mathbf{x}}_s \rangle \langle \tilde{\mathbf{x}}_s \mid \mathfrak{D}_s \mid \mathbf{x} \rangle \quad (24)$$

where \mathfrak{D}_s is the operator that forward diffuses a delta function at \mathbf{x} to time s under Eq. (2), and \mathfrak{D}_s^\dagger brings each $\tilde{\mathbf{x}}_s$ back to $s = 0$ according to Eq. (3). The average over \mathbf{x}' is the denoised mean $\hat{\mathbf{x}}(\tilde{\mathbf{x}}_s)$, toward which the score function at s points (cf. Eq. (44)). The integral over time and space aggregates all the $\mathbf{x} \rightarrow \mathbf{x}'$ transitions mediated by every possible $\tilde{\mathbf{x}}_s$.

In quantum mechanics, transition rates take a form similar to Eq. (24), with the \mathfrak{D}_s operators replaced by the interaction term in the model. These rates are used to compute scattering cross-sections, which can be measured experimentally. This is how physicists test whether their theoretical model matches reality. If the predictions fail to agree with experiments, they must go back and construct a better model. The training of a diffusion model mirrors this procedure—given the training samples, which are observations from reality, we construct a model and iteratively refine it till it fits the data.

Writing Eq. (22) in the Dirac form, Eq. (24), allows us to interpret each $\mathbf{x} \rightarrow \mathbf{x}'$ transformation as an autoencoding step. That is, \mathfrak{D}_s encodes $|\mathbf{x}\rangle$ into the intermediate states $|\tilde{\mathbf{x}}_s\rangle$, which can be viewed as a latent. Since forward diffusion is dissipative, $|\tilde{\mathbf{x}}_s\rangle$ contains less information than $|\mathbf{x}\rangle$, so \mathfrak{D}_s is the first half of an information bottleneck (see Sec. A.2). On the other hand \mathfrak{D}_s^\dagger decodes $|\tilde{\mathbf{x}}_s\rangle$ back to $|\mathbf{x}'\rangle$, the reconstructed version of $|\mathbf{x}\rangle$. At larger s the latent is less informative, and only the high-level details can be reconstructed. Thus, the integral over s implies that *a diffusion model is an infinite tower of variational autoencoders*, each capturing information at a different level of abstraction from the signal $|\mathbf{x}\rangle$. Shallower autoencoders in the tower, the ones at small s , capture the perceptual detail in the images, whereas the deeper ones retain the semantic features. We scan this tower with a DAE in Sec. E.

In stochastic thermodynamics, $-\log p_d(\mathbf{x})$ is interpreted as the sum total of the *path entropies* of each trajectory that starts from p_0 and ends at \mathbf{x} (Seifert, 2005). That is, it measures the accumulated

information from all different ways of arriving at \mathbf{x} at time T . This is yet another interpretation of Eq. (24): given a test sample \mathbf{x} , we corrupt it by different degrees and aggregate the log probabilities of all paths that travel back to \mathbf{x} —it is proportional to the distance squared from the mean $\hat{\mathbf{x}}(\tilde{\mathbf{x}}_s)$ of reverse diffusion landings \mathbf{x}' . Thus, the geometric and entropic viewpoints converge.

It should be pointed out that our perspective differs from the one in Huang et al. (2021), where a diffusion model is viewed as a *single* infinitely deep autoencoder. They divide the time interval $(0, T]$ into infinitesimal steps, which are then interpreted as stochastic layers of this autoencoder. In contrast, Eq. (24) decomposes the diffusion model into a multitude of autoencoders, each one trying to reconstruct the signal at a different noise scale. This viewpoint aligns more closely with the simulation-free training of such models (Lipman et al., 2023). Furthermore, the autoencoders are not independent from one another—an encoder-decoder pair at scale s receives a subset of the information that flows through a pair at an earlier s . A harmonious synthesis of these two pictures is to view a diffusion model as the continuum limit of an autoencoder with *skip connections*, like a U-net (Ronneberger et al., 2015).

Finally, note that the above picture can be extended to conditional probabilities by simply replacing the marginal density with the conditional one everywhere. That is, $-\log p_d(\mathbf{x}|\mathbf{y})$ will be smaller if the denoised means $\hat{\mathbf{x}}(\tilde{\mathbf{x}}_s|\mathbf{y})$ are closer to \mathbf{x} , which is the case for conditional densities that assign high probability to regions close to \mathbf{x} .

7 CONCLUSION

Diffusion models are a natural bridge between information theory and generative modeling. In this work, we highlighted mutual information as a unifying concept that connects several aspects of diffusion models such as conditioning, neural storage capacity, guidance, latent representations, and the structure of image data. We saw in Sec. 3 the complementary nature of memory and compute. In Sec. 4 we argued that CFG strengthens the binding between signal by steering the denoising process along directions of increasing mutual information. CFG serves as a heuristic to overcome the inherently low mutual information between images and their labels, which in turn is a manifestation of the low intrinsic dimensionality of the data manifold. In doing so, however, CFG also distorts the manifold itself (see Fig. 1).

The information-theoretic perspective offers a principled approach to studying and potentially resolving the problem. By letting the diffusion model develop its own side information we can (i) peer inside the model and examine the hierarchical structure of the information stored in the network (see Sec. E), and (ii) create an intermediate latent variable that binds more strongly with the images as well as their labels and acts as an intermediary between the two. In Preechakul et al. (2022), a second diffusion model relates \mathbf{Y} to \mathbf{Z} , which then conditions the image diffusion model. A variation of the same idea is applied in Rombach et al. (2022); Vahdat et al. (2021), where diffusion operates only on \mathbf{Z} while perceptual detail is delegated to a separate autoencoder. In Sec. 6, we framed diffusion models as an infinite hierarchy of autoencoders that progressively resolve finer details of the signal. From this perspective, it becomes clear why replacing the shallow autoencoders—those responsible for shouldering the bulk of the information load needed to extract the minutiae of image vectors—can be especially beneficial.

During forward diffusion, a part of the information loss is due to the de-correlation between the components of \mathbf{X} as the distribution thermalizes. These correlations are re-established in the generative step, and quantified by the total correlation term $\text{TC}(\mathbf{X})$ in Eq. (11). This is also the term that diverges if \mathbf{X} resides on a lower-dimensional manifold (see discussion near Fig. 3). Accordingly, the pronounced peaks in the neural entropy profiles of image diffusion models provide additional evidence for the manifold hypothesis (Brown et al., 2023) (see Fig. 8).

As a final remark, we stress that core ideas in this work also apply to discrete diffusion processes, although effort needs to be put in to find the analogous expressions for neural entropy and mutual information. Discrete diffusion is particularly relevant in the context of language modeling (Lou et al., 2024b; Xu et al., 2024). In this setting pixels are replaced by text tokens, and entire sequences are generated in parallel, in contrast to the sequential decoding of autoregressive models. Whether inter-token correlations share the properties of image data remains an intriguing direction for study.

REFERENCES

Alexander A. Alemi, Ian Fischer, Joshua V. Dillon, and Kevin Murphy. Deep variational information bottleneck. *CoRR*, abs/1612.00410, 2016. URL <http://arxiv.org/abs/1612.00410>. 16

Christopher M. Bishop. *Pattern Recognition and Machine Learning*. Information Science and Statistics. Springer, New York, 2006. ISBN 978-0387310732. 18, 20, 22

James Bradbury, Roy Frostig, Peter Hawkins, Matthew James Johnson, Chris Leary, Dougal Maclaurin, George Necula, Adam Paszke, Jake VanderPlas, Skye Wanderman-Milne, and Qiao Zhang. JAX: composable transformations of Python+NumPy programs, 2018. URL <http://github.com/jax-ml/jax>. 20

Arwen Bradley and Preetum Nakkiran. Classifier-free guidance is a predictor-corrector. In *NeurIPS Workshop on Score-Based Methods*, 2024. URL <https://arxiv.org/abs/2408.09000>. 19

Bradley C. A. Brown, Anthony L. Caterini, Brendan Leigh Ross, Jesse C. Cresswell, and Gabriel Loaiza-Ganem. Verifying the union of manifolds hypothesis for image data. In *The Eleventh International Conference on Learning Representations, ICLR 2023, Kigali, Rwanda, May 1-5, 2023*. OpenReview.net, 2023. URL <https://openreview.net/forum?id=Rvee9CAX4fi>. 9

Raphaël Chetrite, Paolo Muratore-Ginanneschi, and Kay Schwieger. E. Schrödinger's 1931 paper "On the Reversal of the Laws of Nature" [Über die Umkehrung der Naturgesetze", Sitzungsberichte der preussischen Akademie der Wissenschaften, physikalisch-mathematische Klasse, 8 N9 144–153]. *The European Physical Journal H*, 46(1):28, Nov 2021. ISSN 2102-6467. doi: 10.1140/epjh/s13129-021-00032-7. URL <https://doi.org/10.1140/epjh/s13129-021-00032-7>. 3

Kevin Clark and Priyank Jaini. Text-to-Image Diffusion Models are Zero-Shot Classifiers. In Alice Oh, Taesup Naumann, Amir Globerson, Kate Saenko, Moritz Hardt, and Sergey Levine (eds.), *Advances in Neural Information Processing Systems*, volume 36, pp. 58921–58937. Curran Associates, Inc., 2023. URL https://proceedings.neurips.cc/paper_files/paper/2023/file/b87bdcf963cad3d0b265fcb78ae7d11e-Paper-Conference.pdf. 5, 28

Thomas M. Cover and Joy A. Thomas. *Elements of Information Theory (Wiley Series in Telecommunications and Signal Processing)*. Wiley-Interscience, USA, 2006. ISBN 0471241954. 1, 2, 16

Prafulla Dhariwal and Alexander Nichol. Diffusion models beat gans on image synthesis. In M. Ranzato, A. Beygelzimer, Y. Dauphin, P.S. Liang, and J. Wortman Vaughan (eds.), *Advances in Neural Information Processing Systems*, volume 34, pp. 8780–8794. Curran Associates, Inc., 2021. URL https://proceedings.neurips.cc/paper_files/paper/2021/file/49ad23d1ec9fa4bd8d77d02681df5cfa-Paper.pdf. 1, 5

Bradley Efron. Tweedie's formula and selection bias. *Journal of the American Statistical Association*, 106(496):1602–1614, 2011. 18

Giulio Franzese, Mustapha Bounoua, and Pietro Michiardi. MINDE: Mutual information neural diffusion estimation. In *Proceedings of the International Conference on Learning Representations (ICLR)*, pp. 16685–16716, 2024. URL https://proceedings.iclr.cc/paper_files/paper/2024/file/47f75e809409709c6d226ab5ca0c9703-Paper-Conference.pdf. 5, 19

Hao Ge and Da-Quan Jiang. Generalized jarzynski's equality of inhomogeneous multidimensional diffusion processes. *Journal of Statistical Physics*, 131(4):675–689, 5 2008. ISSN 1572-9613. doi: 10.1007/s10955-008-9520-4. URL <https://doi.org/10.1007/s10955-008-9520-4>. 17

Irina Higgins, Loïc Matthey, Arka Pal, Christopher P. Burgess, Xavier Glorot, Matthew M. Botvinick, Shakir Mohamed, and Alexander Lerchner. β -vae: Learning basic visual concepts with a constrained variational framework. In *5th International Conference on Learning Representations, ICLR 2017, Toulon, France, April 24-26, 2017, Conference Track Proceedings*. Open-Review.net, 2017. URL <https://openreview.net/forum?id=Sy2fzU9gl>. 6

Jonathan Ho and Tim Salimans. Classifier-free diffusion guidance. *CoRR*, abs/2207.12598, 2022. doi: 10.48550/ARXIV.2207.12598. URL <https://doi.org/10.48550/arXiv.2207.12598>. 1, 5, 20

Jonathan Ho, Ajay Jain, and Pieter Abbeel. Denoising diffusion probabilistic models. In Hugo Larochelle, Marc'Aurelio Ranzato, Raia Hadsell, Maria-Florina Balcan, and Hsuan-Tien Lin (eds.), *Advances in Neural Information Processing Systems 33: Annual Conference on Neural Information Processing Systems 2020, NeurIPS 2020, December 6-12, 2020, virtual*, 2020. URL <https://proceedings.neurips.cc/paper/2020/hash/4c5bcfec8584af0d967f1ab10179ca4b-Abstract.html>. 18

Chin-Wei Huang, Jae Hyun Lim, and Aaron C. Courville. A variational perspective on diffusion-based generative models and score matching. In Marc'Aurelio Ranzato, Alina Beygelzimer, Yann N. Dauphin, Percy Liang, and Jennifer Wortman Vaughan (eds.), *Advances in Neural Information Processing Systems 34: Annual Conference on Neural Information Processing Systems 2021, NeurIPS 2021, December 6-14, 2021, virtual*, pp. 22863–22876, 2021. URL <https://proceedings.neurips.cc/paper/2021/hash/c11abfd29e4d9b4d4b566b01114d8486-Abstract.html>. 9, 17

David A. Huffman. A method for the construction of minimum-redundancy codes. *Proceedings of the IRE*, 40(9):1098–1101, 1952. doi: 10.1109/JRPROC.1952.273898. 8

Zahra Kadkhodaie, Florentin Guth, Eero P. Simoncelli, and Stéphane Mallat. Generalization in diffusion models arises from geometry-adaptive harmonic representation. *CoRR*, abs/2310.02557, 2023. doi: 10.48550/ARXIV.2310.02557. URL <https://doi.org/10.48550/arXiv.2310.02557>. 7

Tero Karras, Miika Aittala, Timo Aila, and Samuli Laine. Elucidating the Design Space of Diffusion-Based Generative Models. In Sanmi Koyejo, S. Mohamed, A. Agarwal, Danielle Belgrave, K. Cho, and A. Oh (eds.), *Advances in Neural Information Processing Systems 35: Annual Conference on Neural Information Processing Systems 2022, NeurIPS 2022, New Orleans, LA, USA, November 28 - December 9, 2022*, 2022. URL http://papers.nips.cc/paper_files/paper/2022/hash/a98846e9d9cc01cfb87eb694d946ce6b-Abstract-Conference.html. 18

J. L. Kelly. A New Interpretation of Information Rate. *The Bell System Technical Journal*, 35(4): 917–926, 1956. doi: 10.1002/j.1538-7305.1956.tb03809.x. 1, 2

Diederik Kingma and Ruiqi Gao. Understanding Diffusion Objectives as the ELBO with Simple Data Augmentation. In A. Oh, T. Naumann, A. Globerson, K. Saenko, M. Hardt, and S. Levine (eds.), *Advances in Neural Information Processing Systems*, volume 36, pp. 65484–65516. Curran Associates, Inc., 2023. URL https://proceedings.neurips.cc/paper_files/paper/2023/file/ce79fbf9baef726645bc2337abb0ade2-Paper-Conference.pdf. 19

Diederik P. Kingma and Max Welling. Auto-encoding variational bayes. In Yoshua Bengio and Yann LeCun (eds.), *2nd International Conference on Learning Representations, ICLR 2014, Banff, AB, Canada, April 14-16, 2014, Conference Track Proceedings*, 2014. URL <http://arxiv.org/abs/1312.6114>. 6, 16, 17

Alex Krizhevsky. Learning multiple layers of features from tiny images. Technical report, University of Toronto, 2009. <https://www.cs.toronto.edu/~kriz/learning-features-2009-TR.pdf>. 20

Yann LeCun, Léon Bottou, Yoshua Bengio, and Patrick Haffner. Gradient-based learning applied to document recognition. *Proceedings of the IEEE*, 86(11):2278–2324, 1998. doi: 10.1109/5.726791. 20

Alexander C. Li, Mihir Prabhudesai, Shivam Duggal, Ellis Brown, and Deepak Pathak. Your diffusion model is secretly a zero-shot classifier. In *Proceedings of the IEEE/CVF International Conference on Computer Vision (ICCV)*, pp. 2206–2217, October 2023. 5, 28

Marvin Li and Sitan Chen. Critical windows: Non-asymptotic theory for feature emergence in diffusion models. In *Proceedings of the 41st International Conference on Machine Learning (ICML)*, ICML’24, pp. 1097:1–1097:25. JMLR.org, 2024. 28

Yaron Lipman, Ricky T. Q. Chen, Heli Ben-Hamu, Maximilian Nickel, and Matthew Le. Flow matching for generative modeling. In *The Eleventh International Conference on Learning Representations, ICLR 2023, Kigali, Rwanda, May 1-5, 2023*. OpenReview.net, 2023. URL <https://openreview.net/forum?id=PqvMRDCJT9t>. 9

Aaron Lou, Chenlin Meng, and Stefano Ermon. Discrete diffusion modeling by estimating the ratios of the data distribution. In *Forty-first International Conference on Machine Learning, ICML 2024, Vienna, Austria, July 21-27, 2024*. OpenReview.net, 2024a. URL <https://openreview.net/forum?id=CNicRIVIPA>. 1

Aaron Lou, Chenlin Meng, and Stefano Ermon. Discrete diffusion modeling by estimating the ratios of the data distribution. In *Forty-first International Conference on Machine Learning, ICML 2024, Vienna, Austria, July 21-27, 2024*. OpenReview.net, 2024b. URL <https://openreview.net/forum?id=CNicRIVIPA>. 9

David J. C. MacKay. *Information Theory, Inference & Learning Algorithms*. Cambridge University Press, USA, 2002. ISBN 0521642981. 2

Dimitra Maoutsa, Sebastian Reich, and Manfred Opper. Interacting particle solutions of fokker–planck equations through gradient–log–density estimation. *Entropy*, 22(8):802, 2020. doi: 10.3390/e22080802. URL <https://www.mdpi.com/1099-4300/22/8/802>. 21

Koichi Miyasawa. An empirical Bayes estimator of the mean of a normal population. *Bulletin of the International Statistical Institute*, 38:181–188, 1961. 18

Shen Nie, Fengqi Zhu, Zebin You, Xiaolu Zhang, Jingyang Ou, Jun Hu, Jun Zhou, Yankai Lin, Ji-Rong Wen, and Chongxuan Li. Large Language Diffusion Models, 2025. URL <https://arxiv.org/abs/2502.09992>. 1

Michele Pavon. Stochastic control and nonequilibrium thermodynamical systems. *Applied Mathematics and Optimization*, 19(1):187–202, 1989. doi: 10.1007/BF01448198. URL <https://doi.org/10.1007/BF01448198>. 17

Konpat Preechakul, Nattanat Chatthee, Suttisak Wizadwongsa, and Supasorn Suwajanakorn. Diffusion Autoencoders: Toward a Meaningful and Decodable Representation. In *Proceedings of the IEEE/CVF Conference on Computer Vision and Pattern Recognition (CVPR)*, pp. 10619–10629, June 2022. 6, 9

Akhil Premkumar. Neural Entropy, 2025. URL <https://arxiv.org/abs/2409.03817>. 1, 3, 4, 17

R. Tyrrell Rockafellar and Roger J.-B. Wets. *Variational analysis / R. Tyrrell Rockafellar, Roger J.-B. Wets*. Grundlehren der mathematischen Wissenschaften, 317. Springer, Berlin ;, 1998. ISBN 3540627723. URL <http://swbplus.bsz-bw.de/bsz063165805cov.htm>. 17

Robin Rombach, Andreas Blattmann, Dominik Lorenz, Patrick Esser, and Björn Ommer. High-resolution image synthesis with latent diffusion models. In *IEEE/CVF Conference on Computer Vision and Pattern Recognition, CVPR 2022, New Orleans, LA, USA, June 18-24, 2022*, pp. 10674–10685. IEEE, 2022. doi: 10.1109/CVPR52688.2022.01042. URL <https://doi.org/10.1109/CVPR52688.2022.01042>. 9

Olaf Ronneberger, Philipp Fischer, and Thomas Brox. U-net: Convolutional networks for biomedical image segmentation. *CoRR*, abs/1505.04597, 2015. URL <http://arxiv.org/abs/1505.04597>. 9

D. L. Ruderman. The statistics of natural images. *Network: Computation in Neural Systems*, 5(4): 517–548, November 1994. doi: 10.1088/0954-898X/5/4/006. URL <https://dx.doi.org/10.1088/0954-898X/5/4/006>. 25

J. J. Sakurai and Jim Napolitano. *Modern Quantum Mechanics*. Cambridge University Press, Cambridge, 3 edition, 2020. 8

Tim Salimans and Jonathan Ho. Progressive distillation for fast sampling of diffusion models. *CoRR*, abs/2202.00512, 2022. URL <https://arxiv.org/abs/2202.00512>. 20

Udo Seifert. Entropy production along a stochastic trajectory and an integral fluctuation theorem. *Phys. Rev. Lett.*, 95:040602, Jul 2005. doi: 10.1103/PhysRevLett.95.040602. URL <https://link.aps.org/doi/10.1103/PhysRevLett.95.040602>. 8

Udo Seifert. Stochastic Thermodynamics, Fluctuation Theorems and Molecular Machines. *Reports on Progress in Physics*, 75(12):126001, Nov 2012. doi: 10.1088/0034-4885/75/12/126001. URL <https://dx.doi.org/10.1088/0034-4885/75/12/126001>. 3

C. E. Shannon. A mathematical theory of communication. *The Bell System Technical Journal*, 27(3):379–423, 1948. doi: 10.1002/j.1538-7305.1948.tb01338.x. 1

David Slepian and Jack Wolf. Noiseless coding of correlated information sources. *IEEE Transactions on Information Theory*, 19(4):471–480, 1973. doi: 10.1109/TIT.1973.1055037. 4

Jascha Sohl-Dickstein, Eric Weiss, Niru Maheswaranathan, and Surya Ganguli. Deep unsupervised learning using nonequilibrium thermodynamics. In Francis Bach and David Blei (eds.), *Proceedings of the 32nd International Conference on Machine Learning*, volume 37 of *Proceedings of Machine Learning Research*, pp. 2256–2265, Lille, France, 07–09 Jul 2015. PMLR. URL <https://proceedings.mlr.press/v37/sohl-dickstein15.html>. 1, 20

Yang Song, Conor Durkan, Iain Murray, and Stefano Ermon. Maximum Likelihood Training of Score-Based Diffusion Models. In Marc’Aurelio Ranzato, Alina Beygelzimer, Yann N. Dauphin, Percy Liang, and Jennifer Wortman Vaughan (eds.), *Advances in Neural Information Processing Systems 34: Annual Conference on Neural Information Processing Systems 2021, NeurIPS 2021, December 6-14, 2021, virtual*, pp. 1415–1428, 2021a. URL <https://proceedings.neurips.cc/paper/2021/hash/0a9fdbb17feb6ccb7ec405cfb85222c4-Abstract.html>. 17, 19

Yang Song, Jascha Sohl-Dickstein, Diederik P. Kingma, Abhishek Kumar, Stefano Ermon, and Ben Poole. Score-Based Generative Modeling through Stochastic Differential Equations. In *9th International Conference on Learning Representations, ICLR 2021, Virtual Event, Austria, May 3-7, 2021*. OpenReview.net, 2021b. URL <https://openreview.net/forum?id=PxTIG12RRHS>. 1, 7, 20

Edward O. Thorp. The Kelly Criterion in Blackjack Sports Betting, and the Stock Market. In Leonard C MacLean, Edward O Thorp, and William T Ziemba (eds.), *THE KELLY CAPITAL GROWTH INVESTMENT CRITERION THEORY and PRACTICE*, World Scientific Book Chapters, chapter 54, pp. 789–832. World Scientific Publishing Co. Pte. Ltd., April 2011. URL https://ideas.repec.org/h/wsi/wschap/9789814293501_0054.html. 2

Naftali Tishby, Fernando C. N. Pereira, and William Bialek. The Information Bottleneck Method. *CoRR*, physics/0004057, 2000. URL <http://arxiv.org/abs/physics/0004057>. 16

Arash Vahdat, Karsten Kreis, and Jan Kautz. Score-based Generative Modeling in Latent Space. In Marc’Aurelio Ranzato, Alina Beygelzimer, Yann Dauphin, Percy Liang, and Jennifer Wortman Vaughan (eds.), *Advances in Neural Information Processing Systems*, volume 34, pp. 11287–11302. Curran Associates, Inc., 2021. URL https://proceedings.neurips.cc/paper_files/paper/2021/file/5dca4c6b9e244d24a30b4c45601d9720-Paper.pdf. 9

S. Vaikuntanathan and C. Jarzynski. Dissipation and Lag in Irreversible Processes. *Europhysics Letters*, 87(6):60005, oct 2009. doi: 10.1209/0295-5075/87/60005. URL <https://dx.doi.org/10.1209/0295-5075/87/60005>. 3

Laurens van der Maaten and Geoffrey Hinton. Visualizing data using t-sne. *Journal of Machine Learning Research*, 9(86):2579–2605, 2008. URL <http://jmlr.org/papers/v9/vandermaaten08a.html>. 28

Zhou Wang and Alan C. Bovik. Mean Squared Error: Love It or Leave It? A New Look at Signal Fidelity Measures. *IEEE Signal Processing Magazine*, 26(1):98–117, 2009. doi: 10.1109/MSP.2008.930649. 22

Satosi Watanabe. Information theoretical analysis of multivariate correlation. *IBM Journal of Research and Development*, 4(1):66–82, 1960. doi: 10.1147/rd.41.0066. 4

Minkai Xu, Tomas Geffner, Karsten Kreis, Weili Nie, Yilun Xu, Jure Leskovec, Stefano Ermon, and Arash Vahdat. Energy-based diffusion language models for text generation. *CoRR*, abs/2410.21357, 2024. doi: 10.48550/ARXIV.2410.21357. URL <https://doi.org/10.48550/arXiv.2410.21357>. 9

Yilun Xu, Shengjia Zhao, Jiaming Song, Russell Stewart, and Stefano Ermon. A theory of usable information under computational constraints. In *8th International Conference on Learning Representations, ICLR 2020, Addis Ababa, Ethiopia, April 26-30, 2020*. OpenReview.net, 2020. URL <https://openreview.net/forum?id=r1eBeyHFDH>. 4

Candi Zheng and Yuan Lan. Characteristic guidance: Non-linear correction for diffusion model at large guidance scale. In *Forty-first International Conference on Machine Learning, ICML 2024, Vienna, Austria, July 21-27, 2024*. OpenReview.net, 2024. URL <https://openreview.net/forum?id=eOtjMYdGLt>. 19

A INFORMATION THEORY

A.1 MUTUAL INFORMATION: A PRIMER

The mutual information between two random variables quantifies the reduction in uncertainty of one variable given the value of the other variable. If X and Y are the random variables in question, then the mutual information $I(X; Y)$ is the information gained about X through a measurement of Y . If $p(x, y)$ is the joint distribution of X and Y and $p(x)$ and $p(y)$ are the marginals,

$$\begin{aligned} I(X; Y) &:= D_{\text{KL}}(p(x, y) \| p(x)p(y)) \\ &= S(X) - S(X|Y) = S(Y) - S(Y|X). \end{aligned} \quad (25)$$

By construction, $I(X; Y)$ is symmetric in its arguments, and it is non-negative. Mutual information captures *all* forms of statistical dependence, not just linear ones. That said, it is easier to develop some intuition for $I(X; Y)$ by considering a simple linear model

$$Y = aX + \varepsilon, \quad (26)$$

where $X \sim \mathcal{N}(0, \sigma_X^2)$, $\varepsilon \sim \mathcal{N}(0, \sigma_\varepsilon^2)$, and a is a real constant. It is easy to see that

$$Y|X = x \sim \mathcal{N}(ax, \sigma_\varepsilon^2), \quad (27a)$$

$$Y \sim \mathcal{N}(0, a^2\sigma_X^2 + \sigma_\varepsilon^2), \quad (27b)$$

$$X|Y = y \sim \mathcal{N}\left(\frac{a\sigma_X^2}{a^2\sigma_X^2 + \sigma_\varepsilon^2}y, \frac{\sigma_X^2\sigma_\varepsilon^2}{a^2\sigma_X^2 + \sigma_\varepsilon^2}\right), \quad (27c)$$

where Eq. (27a) follows from the fact that Y is a scaled version of X with some noise added to it, and Eq. (27b) is obtained by marginalizing this distribution over X . With these distributions, Eq. (27c) can be derived using Bayes' rule. Notice that $X|Y$ has a smaller variance than X . This is what we mean when we say $p(x|y)$ is ‘narrower’ than $p(x)$ (see Fig. 2), although for general distributions this is only true *on average*—there can be cases where the conditional is broader than the marginal for some y .

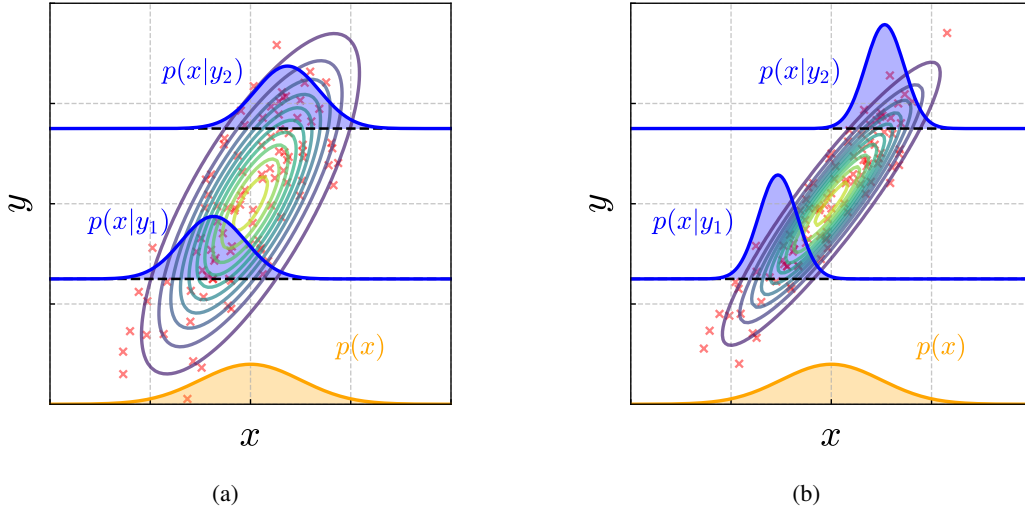


Figure 2: The linear Gaussian model from Eq. (26) with (a) higher noise/larger σ_ε , and (b) lower noise/smaller σ_ε . The blue curves are the conditionals $X|Y = y$ for some y , and the orange curve is the marginal over X . Notice how the conditionals have a tighter variance compared to the marginal. The contours are surfaces over constant probability in the joint distribution, and the red markers are some samples.

The main point is that knowing Y dispels some of the uncertainty in X . That is, $X|Y = y$ has a lower entropy on average than X ,

$$S(X|Y) = \int dy p(y) S(X|Y = y) = - \int dy p(y) \int dx p(x|y) \log p(x|y) \leq S(X). \quad (28)$$

Mutual information is the difference between these two entropies. We can compute the latter explicitly from Eqs. (27a) and (27b),

$$I(X;Y) = S(Y) - S(Y|X) = \frac{1}{2} \log \frac{\text{Var}(Y)}{\text{Var}(Y|X)} = \frac{1}{2} \log \left(1 + \frac{a^2 \sigma_X^2}{\sigma_\varepsilon^2} \right). \quad (29)$$

Notice that $I(X;Y) \rightarrow 0$ as $\sigma_\varepsilon \gg \sigma_X$, since the X signal is drowned out by the noise in this regime. In the opposite limit, when noise is very weak, X and Y are very strongly correlated and $I(X;Y)$ grows. If X and Y were discrete random variables $I(X;Y)$ would have saturated at $S(X)$. However, in the continuous case mutual information can diverge to infinity, which is the same pathology shared by differential entropy (Cover & Thomas, 2006, Chap. 8). Indeed, in the noiseless limit $p(x,y)$ collapses onto the line $y = ax$ whereas the product $p(x)p(y)$ spreads mass over the whole plane, so $p(x,y)$ is singular with respect to $p(x)p(y)$ in Eq. (25) (see Fig. 5).

This peculiar behavior of $I(X;Y)$ in the continuous case is reminiscent of the singular growth in entropy in image diffusion models as $t \rightarrow T$ (see Fig. 8). It is in fact the same phenomenon, which arises when the joint distribution converges on a lower dimensional manifold in the noiseless limit (see Fig. 3). In diffusion models the piece that becomes singular is the total correlation term in Eq. (11), $\text{TC}(\mathbf{X})$, which is a generalization of mutual information. We shall show in Sec. E.2 that the re-establishment of perceptual detail in the images coincides with a sharp peak of the neural entropy rate at the final stages of the generative process. Correlations between nearby pixels must be made very tight to get these small-scale details correct, which forces the image vector to track a manifold of lower dimensions, resulting in a divergent $\text{TC}(\mathbf{X})$. This is why the small details of the image take up a sizable portion of the total information budget.

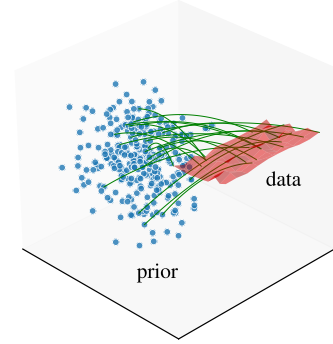


Figure 3

A.2 THE INFORMATION BOTTLENECK

Consider the problem of building a classifier that maps an input X to a label Y , where Y is now a discrete random variable. We would like to find a representation Z of X that captures all information in X that is relevant to predicting Y , while discarding the superfluous details. This is the viewpoint formalized by the information bottleneck, where the optimal assignment from X to Z is obtained by varying the stochastic map $q(z|x)$ to solve

$$\min_{q(z|x)} I(X;Z) - \gamma^{-1} I(Z;Y), \quad (30)$$

with $\gamma > 0$. A rigorous derivation of this functional is given in Tishby et al. (2000), but the intuition behind it is simple: minimizing $I(X;Z)$ maps a wide range of X values to a narrow range of the latent variable Z , and maximizing $I(Z;Y)$ creates a map between Z and Y where knowing Z almost completely determines Y . This forces $q(z|x)$ to only encode features from X into Z that most strongly associate with the class label Y , which is a form of selective compression. By adjusting γ we can set the tradeoff between compression and information preservation—setting $\gamma = 0$ collapses $q(z|x)$ to a single point, whereas $\gamma \rightarrow \infty$ pushes maximal detail from X to Z .

In general, Y can be any random variable, including a reconstruction of X itself. This is an autoencoder. However, there are a few subtle differences between Eq. (30) and the standard formulation of autoencoders (Kingma & Welling, 2014; Alemi et al., 2016). To see the connection we expand Eq. (30) to

$$\min_{q(z|x)} S(Z) - S(Z|X) - \gamma^{-1} (S(Y) - S(Y|Z)). \quad (31)$$

The entropy of Y is independent of the encoder, so we can drop it from the objective (cf. Eq. (20)). We can introduce a regularization term to make the Z distribution close to a prior $p(z)$, like a standard normal distribution. This controls the entropy of Z from becoming too large as we vary $q(z|x)$. With these modifications Eq. (31) becomes

$$\min_{q(z|x)} \mathbb{E}_y \mathbb{E}_{q(z|x)} [-\log p(y|z)] + \gamma \mathbb{E}_x D_{\text{KL}}(q(z|x) \parallel p(z)). \quad (32)$$

Setting $Y = X$, we recover the negative ELBO from Eq. (17).

B STOCHASTIC CONTROL

B.1 LOG LIKELIHOOD BOUND

In Sec. 3 we introduced the forward and reverse SDEs, Eqs. (2) and (3), which takes $p_d \rightarrow p_0$ and back. If we replace the reverse process with an SDE (see Fig. 11)

$$d\mathbf{X}_t = -\mathbf{u}(\mathbf{X}_t, t)dt + \sigma(T-t)d\mathbf{B}_t, \quad (33)$$

and distribution $p_u(\cdot, 0)$ at time $t = 0$ evolves to $p_u(\cdot, T)$ at $t = T$, the log density of which is bound as (see Premkumar, 2025, App. E.2)

$$-\log p_u(\mathbf{x}, T) \leq \mathbb{E} \left[\left(\int_0^T ds \frac{\|b_+ - \mathbf{u}\|^2}{2\sigma^2} + \mathbf{u} \cdot \nabla \log p(\tilde{\mathbf{x}}_s, s | \tilde{\mathbf{x}}_0, 0) \right) - \log p_u(\tilde{\mathbf{x}}_T, 0) \middle| \tilde{\mathbf{X}}_0 = \mathbf{x} \right]. \quad (34)$$

The expectation value is taken over all trajectories generated by Eq. (2), starting at $\tilde{\mathbf{X}}_0 = \mathbf{x}$. This inequality, which can be derived from optimal control theory (Pavon, 1989), or the Feynman-Kac formula (Ge & Jiang, 2008; Huang et al., 2021), will be the starting point of many of our derivations. Completing the square, the bound can be written as

$$\begin{aligned} -\log p_u(\mathbf{x}, T) &\leq \int_0^T ds \frac{1}{2\sigma^2} \mathbb{E} \left[\|b_+ - \sigma^2 \nabla \log p(\tilde{\mathbf{x}}_s, s | \tilde{\mathbf{x}}_0, 0) - \mathbf{u}\|^2 \middle| \tilde{\mathbf{X}}_0 = \mathbf{x} \right] \\ &\quad - \int_0^T ds \mathbb{E} \left[\frac{\sigma^2}{2} \|\nabla \log p(\tilde{\mathbf{x}}_s, s | \tilde{\mathbf{x}}_0, 0)\|^2 + \nabla \cdot b_+ \middle| \tilde{\mathbf{X}}_0 = \mathbf{x} \right] + S_0. \end{aligned} \quad (35)$$

We have replaced $\mathbb{E}[-\log p_u(\tilde{\mathbf{x}}_T)]$ with the negative differential entropy $S_0 := \mathbb{E}_{p_0}[-\log p_0]$ by choosing $p_u(\cdot, 0)$ to be $p_0(\cdot)$ and noting that, to a very good approximation, $\tilde{\mathbf{x}}_T$ would be distributed as p_0 irrespective of the \mathbf{x} at which it started.

Averaging Eq. (35) over the data distribution p_d yields an upper bound on the cross-entropy between p_d and the reconstructed distribution $p_u(\cdot, T)$. In a diffusion model a neural network parametrizes the *control* \mathbf{u} , which affects only one term in the bound. Therefore, minimizing the cross-entropy is equivalent to minimizing the *denoising* objective

$$\mathbb{E}_{\mathbf{X}}[-\log p_u(\mathbf{x}, T)] + c \leq \int_0^T ds \frac{1}{2\sigma^2} \mathbb{E}_{\mathbf{X}, \tilde{\mathbf{X}}_s} \left[\|b_+ - \sigma^2 \nabla \log p(\tilde{\mathbf{x}}_s, s | \mathbf{x}, 0) - \mathbf{u}\|^2 \right] := \mathcal{L}_D, \quad (36)$$

where c denotes the \mathbf{u} -independent terms from Eq. (35), averaged over \mathbf{X} . In an entropy-matching model $\mathbf{u} = -b_+ - \sigma^2 \mathbf{e}_\theta$, so the denoising entropy-matching objective is (cf. Eq. (18))

$$\begin{aligned} \mathbb{E}_{\mathbf{X}}[-\log p_\theta(\mathbf{x}, T)] + c &\leq \\ \int_0^T ds \frac{\sigma^2}{2} \mathbb{E}_{\mathbf{X}, \tilde{\mathbf{X}}_s} \left[\left\| \nabla \log p_{\text{eq}}^{(s)}(\tilde{\mathbf{x}}_s) - \nabla \log p(\tilde{\mathbf{x}}_s, s | \mathbf{x}, 0) + \mathbf{e}_\theta(\tilde{\mathbf{x}}_s, s) \right\|^2 \right] &:= \mathcal{L}_{\text{DEM}}. \end{aligned} \quad (37)$$

A similar objective can be derived for score-matching models by setting $\mathbf{u} = b_+ - \sigma^2 \mathbf{s}_\theta$ in Eq. (36), or equivalently, $\mathbf{s}_\theta = \nabla \log p_{\text{eq}} + \mathbf{e}_\theta$ in Eq. (35) (Song et al., 2021a; Kingma & Welling, 2014).

B.2 OPTIMAL CONTROL AND REGRESSION

The bound in Eq. (34) is saturated by the *optimal control*,

$$\mathbf{u}_* = b_+ - \sigma^2 \nabla \log p, \quad (38)$$

which turns Eq. (33) into the reverse SDE Eq. (3), and the cross-entropy in Eq. (36) reaches its minimum value of $\mathbb{E}_{\mathbf{X}}[-\log p_d]$ (Pavon, 1989; Huang et al., 2021). But that also means \mathbf{u}_* minimizes the denoising objective \mathcal{L}_D ,

$$\mathbf{u}_* = \arg \min_{\mathbf{u}(\cdot, \cdot)} \mathcal{L}_D. \quad (39)$$

We apply Theorem 14.60 of Rockafellar & Wets (1998), which guarantees that the minimization of a time-integrated convex loss functional is achieved by pointwise minimization of the integrand.

Briefly, given a normal integrand \mathcal{J} and a measurable weight function $\lambda(s) \geq 0$, the minimization of \mathcal{J} over the space χ of measurable functions $f : [0, T] \rightarrow \mathbb{R}^{D_{\mathbf{x}}}$ is

$$f_{\star} \in \arg \min_{f(\cdot) \in \chi} \int_0^T ds \lambda(s) \mathcal{J}(s, f(s)) = f_{\star}(s) \Leftrightarrow \arg \min_{f \in \mathbb{R}^{D_{\mathbf{x}}}} \mathcal{J}(s, f), \text{ for almost every } s \in [0, T]. \quad (40)$$

This allows us to analyze the denoising objective independently at each time s , which reduces Eq. (39) to a family of decoupled conditional mean regression problems, each minimizing the expected squared deviation at time s (see Sec. 1.5.5 of Bishop, 2006):

$$\begin{aligned} \mathbf{u}_{\star} &= \arg \min_{\mathbf{u} \in \mathbb{R}^{D_{\mathbf{x}}}} \int d\tilde{\mathbf{x}}_s \int d\mathbf{x} p(\tilde{\mathbf{x}}_s, \mathbf{x}) \|b_+(\tilde{\mathbf{x}}_s) - \sigma^2 \nabla \log p(\tilde{\mathbf{x}}_s, s | \mathbf{x}, 0) - \mathbf{u}(\tilde{\mathbf{x}}_s, s)\|^2 \\ &= b_+(\tilde{\mathbf{x}}_s) - \sigma^2 \mathbb{E}_{\mathbf{x} \sim p(\mathbf{x} | \tilde{\mathbf{x}}_s)} \nabla \log p(\tilde{\mathbf{x}}_s, s | \mathbf{x}, 0). \end{aligned} \quad (41)$$

Comparing with Eq. (38), we conclude that

$$\nabla_{\tilde{\mathbf{x}}_s} \log p(\tilde{\mathbf{x}}_s, s) = \mathbb{E}_{\mathbf{x} \sim p(\mathbf{x} | \tilde{\mathbf{x}}_s)} \nabla_{\tilde{\mathbf{x}}_s} \log p(\tilde{\mathbf{x}}_s, s | \mathbf{x}, 0). \quad (42)$$

If the perturbation kernel is Gaussian,⁴

$$\nabla_{\tilde{\mathbf{x}}_s} \log p(\tilde{\mathbf{x}}_s, s | \mathbf{x}, 0) = -\frac{\tilde{\mathbf{x}}_s - \mu(s)\mathbf{x}}{\Sigma(s)} \quad (43)$$

$$\stackrel{(42)}{\Rightarrow} \nabla_{\tilde{\mathbf{x}}_s} \log p(\tilde{\mathbf{x}}_s, s) = -\frac{\tilde{\mathbf{x}}_s - \mu(s)\mathbb{E}[\mathbf{x} | \tilde{\mathbf{x}}_s]}{\Sigma(s)}, \quad (44)$$

which is the Miyasawa relation/Tweedie's formula (Miyasawa, 1961; Efron, 2011). As mentioned above, Eq. (36) turns into an equality under Eq. (38), with $p_{\mathbf{u}_{\star}}(\cdot, T) = p_{\mathbf{d}}(\cdot)$,

$$\mathbb{E}_{\mathbf{X}}[-\log p_{\mathbf{d}}(\mathbf{x})] + c = \int_0^T ds \frac{\sigma^2}{2} \mathbb{E}_{\mathbf{X}, \tilde{\mathbf{X}}_s} \left[\|\nabla_{\tilde{\mathbf{x}}_s} \log p(\tilde{\mathbf{x}}_s, s) - \nabla \log p(\tilde{\mathbf{x}}_s, s | \mathbf{x}, 0)\|^2 \right]. \quad (45)$$

For the Gaussian kernel, we can substitute Eqs. (43) and (44) and write this as

$$\begin{aligned} \mathbb{E}_{\mathbf{X}}[-\log p_{\mathbf{d}}(\mathbf{x})] + c &= \int_0^T ds \frac{\sigma(s)^2}{2} \frac{\mu(s)^2}{\Sigma(s)^2} \mathbb{E}_{\mathbf{X}, \tilde{\mathbf{X}}_s} \left[\|\mathbb{E}[\mathbf{x} | \tilde{\mathbf{x}}_s] - \mathbf{x}\|^2 \right] \\ &=: \int_0^T ds B(s) \mathbb{E}_{\mathbf{X}, \tilde{\mathbf{X}}_s} \left[\|\hat{\mathbf{x}}(\tilde{\mathbf{x}}_s) - \mathbf{x}\|^2 \right]. \end{aligned} \quad (46)$$

which is Eq. (22) from the main text. In the last step we have collected the time-dependent prefactor into a single function $B(s)$, and defined $\hat{\mathbf{x}}(\tilde{\mathbf{x}}_s) := \mathbb{E}[\mathbf{x} | \tilde{\mathbf{x}}_s]$.

B.3 REWEIGHTED OBJECTIVE

Notice that the choice of weight function $\lambda(s)$ in Eq. (40) does not affect the pointwise minimization that leads to Eq. (42). This provides a theoretical justification of ‘variance dropping’ in practical denoising objectives such as Eq. (37) (Ho et al., 2020). That is, \mathcal{L}_{DEM} is replaced by the Monte Carlo average

$$T \mathbb{E}_{\mathbf{x} \sim p_{\mathbf{d}}} \mathbb{E}_{s \sim \mathcal{U}(0, T)} \left[\lambda(s) \mathbb{E}_{\tilde{\mathbf{x}}_s \sim p(\tilde{\mathbf{x}}_s | \mathbf{x})} \left\| \nabla \log p_{\text{eq}}^{(s)}(\tilde{\mathbf{x}}_s) + \mathbf{e}_{\theta}(\tilde{\mathbf{x}}_s, s) - \nabla \log p(\tilde{\mathbf{x}}_s, s | \mathbf{x}, 0) \right\|^2 \right], \quad (47)$$

⁴The kernel is Gaussian for Ornstein-Uhlenbeck processes, which have the form (Karras et al., 2022)

$$d\tilde{\mathbf{X}}_s = \phi(s) \tilde{\mathbf{X}}_s ds + \sigma(s) d\mathbf{B}_s.$$

The perturbation kernel of this SDE is

$$p(\tilde{\mathbf{x}}_s, s | \mathbf{x}, 0) = \mathcal{N}(\tilde{\mathbf{x}}_s; \mu(s)\mathbf{x}, \Sigma(s)I),$$

where

$$\mu(s) = \exp \left(\int_0^s d\bar{s} \phi(\bar{s}) \right), \quad \Sigma(s) = \mu(s)^2 \int_0^s d\bar{s} \frac{\sigma(\bar{s})^2}{\mu(\bar{s})^2}.$$

where \mathcal{U} is the uniform distribution over $(0, T)$ and $\lambda(s)$ is not necessarily $\sigma^2(s)/2$. Dropping the variance means setting $\lambda(s) = 1$. In principle $\nabla \log p_{\text{eq}} + \mathbf{e}_\theta$ still recovers the optimal score from Eq. (42), but empirical observations show that alternative weighting schemes improve numerical stability and reduce gradient variance (Song et al., 2021a; Kingma & Gao, 2023). We used $\lambda(s) = 1$ in all our image diffusion models, including the DAE decoders. However, when applying Eq. (13) to estimate the mutual information we noticed that choosing $\lambda(s) = \sigma(s)^2/2$ gives slightly more accurate results.

C MUTUAL INFORMATION FROM DIFFUSION

C.1 MINDE

In Sec. 4 we discussed Eq. (13), a formula for mutual information originally derived in Franzese et al. (2024). We will give a derivation of this result using Eq. (34). Setting the control to its optimal value, Eq. (38), and integrating by parts,

$$-\log p_{\text{d}}(\mathbf{x}) = \mathbb{E} \left[\left(\int_0^T ds \frac{\sigma^2}{2} \|\nabla \log p\|^2 - \nabla \cdot (b_+ - \sigma^2 \nabla \log p) \right) - \log p_0(\tilde{\mathbf{x}}_T) \middle| \tilde{\mathbf{X}}_0 = \mathbf{x} \right]. \quad (48)$$

Here $\nabla \log p \equiv \nabla \log p(\tilde{\mathbf{x}}_s, s)$. Averaging this over \mathbf{X} yields the entropy of $p_{\text{d}}(\mathbf{x})$ (cf. Eq. (35)),

$$S(\mathbf{X}) = \mathbb{E}_{\mathbf{X}}[-\log p_{\text{d}}(\mathbf{x})] = \int_0^T ds \mathbb{E}_{\tilde{\mathbf{X}}_s, \mathbf{X}} \left[\frac{\sigma^2}{2} \|\nabla \log p\|^2 - \nabla \cdot (b_+ - \sigma^2 \nabla \log p) \right] + S_0. \quad (49)$$

A similar formula can be derived for $S(\mathbf{X}|\mathbf{Y})$, by changing $\nabla \log p(\tilde{\mathbf{x}}_s, s) \rightarrow \nabla \log p(\tilde{\mathbf{x}}_s, s|\mathbf{y})$ and averaging over \mathbf{y} also. Mutual information is just the difference between the two,

$$\begin{aligned} I(\mathbf{X}; \mathbf{Y}) &= S(\mathbf{X}) - S(\mathbf{X}|\mathbf{Y}) \\ &= \mathbb{E}_{\mathbf{Y}} \left[\int_0^T ds \frac{\sigma^2}{2} \mathbb{E}_{\tilde{\mathbf{X}}_s, \mathbf{X}|\mathbf{y}} \left[\|\nabla \log p(\tilde{\mathbf{x}}_s, s)\|^2 - \|\nabla \log p(\tilde{\mathbf{x}}_s, s|\mathbf{y})\|^2 \right. \right. \\ &\quad \left. \left. + 2\nabla \cdot (\nabla \log p(\tilde{\mathbf{x}}_s, s) - \nabla \log p(\tilde{\mathbf{x}}_s, s|\mathbf{y})) \right] \right] \\ &\stackrel{\text{IBP}}{=} \mathbb{E}_{\mathbf{Y}} \left[\int_0^T ds \frac{\sigma^2}{2} \mathbb{E}_{\tilde{\mathbf{X}}_s, \mathbf{X}|\mathbf{y}} \left[\|\nabla \log p(\tilde{\mathbf{x}}_s, s)\|^2 - \|\nabla \log p(\tilde{\mathbf{x}}_s, s|\mathbf{y})\|^2 \right. \right. \\ &\quad \left. \left. - 2(\nabla \log p(\tilde{\mathbf{x}}_s, s) - \nabla \log p(\tilde{\mathbf{x}}_s, s|\mathbf{y})) \cdot \nabla \log p(\tilde{\mathbf{x}}_s, s|\mathbf{y}) \right] \right] \quad (50) \end{aligned}$$

$$= \mathbb{E}_{\mathbf{Y}} \left[\int_0^T ds \frac{\sigma^2}{2} \mathbb{E}_{\tilde{\mathbf{X}}_s, \mathbf{X}|\mathbf{y}} \left[\|\nabla \log p(\tilde{\mathbf{x}}_s, s|\mathbf{y}) - \nabla \log p(\tilde{\mathbf{x}}_s, s)\|^2 \right] \right]. \quad (51)$$

This is Eq. (13). We have assumed that T is sufficiently large that S_0 is nearly the same in both cases. We also partitioned the expectation over \mathbf{X} into an average over $\mathbf{X}|\mathbf{Y} = \mathbf{y}$ (shortened to $\mathbf{X}|\mathbf{y}$) and over \mathbf{Y} separately. This is why integration by parts in Eq. (50) produced the conditional score term.

C.2 GUIDANCE

The expectation value in Eq. (49) is taken over $p(\tilde{\mathbf{x}}_s, s)$, which is the density forward evolved from the marginal $p_{\text{d}}(\mathbf{x})$. To compute the mutual information between \mathbf{Y} and the CFG-generated \mathbf{X} , we need to compute $S(\mathbf{X}|\mathbf{Y})_{\text{CFG}}$. The CFG modification from Eq. (16) is equivalent to replacing the score with

$$\nabla \log p(\mathbf{x}_t, t|\mathbf{y}) + w \mathbf{s}_{\text{cl}}(\mathbf{y}, t) = \nabla \log \left(\frac{p(\mathbf{x}_t, t|\mathbf{y})^{1+w}}{p(\mathbf{x}_t, t)^w} \right) \quad (52)$$

in Eq. (3). But the resulting SDE is not the reversal of *anything* (Zheng & Lan, 2024; Bradley & Nakkiran, 2024). That is, there is no forward diffusion process for which the intermediate density is $p(\tilde{\mathbf{x}}_s, t|\mathbf{y})^{1+w}/p(\mathbf{x}_t, t)^w$. Therefore, we cannot write down an expression for $S(\mathbf{X}|\mathbf{Y})_{\text{CFG}}$ along the lines of Eq. (49). Consequently, we find no expression analogous to Eq. (51) for mutual information under CFG.

D EXPERIMENTS

We provide empirical evidence of the following claims made in the main text:

1. Conditional diffusion models store an additional amount of information, equal to the mutual information between \mathbf{X} and \mathbf{Y} (see Sec. 3 and Fig. 5). In nats,

$$I(\mathbf{X}; \mathbf{Y}) = S_{\text{tot}}^{\mathbf{X}|\mathbf{Y}} - S_{\text{tot}}^{\mathbf{X}} \approx S_{\text{NN}}^{\mathbf{X}|\mathbf{Y}} - S_{\text{NN}}^{\mathbf{X}}. \quad (53)$$

2. Neural entropy and $I(\mathbf{X}; \mathbf{Y})$ grow rapidly as \mathbf{X} and \mathbf{Y} become more strongly correlated. See discussions at the end of Secs. A.1 and 4 and Fig. 4.
3. CFG increases the mutual information between \mathbf{X} and \mathbf{Y} . See Sec. 4 and Fig. 4.
4. For images, the total information content is dominated by perceptual detail, which erodes rapidly in the first few forward diffusion steps. See Sec. E.1 and Figs. 7 and 8.
5. The perceptual information is largely the same for different image classes. Semantic structure is more closely correlated with the labels. See Sec. E.2 and Fig. 9.

The first three points can be demonstrated with a simple Gaussian model, like the one discussed in Sec. A.1. The mutual information and scores are known analytically, which allows us to compare the theoretical values of different entropies with their estimates from practical diffusion models. Image models are studied in Sec. E, by embedding them inside a DAE.

Our diffusion models used a U-net with self-attention layers (Ho & Salimans, 2022; Salimans & Ho, 2022), and were trained on H200 GPUs with 140 GB of memory. We used JAX/Flax as our ML framework (Bradbury et al., 2018), and trained our image models on the MNIST and CIFAR-10 datasets (LeCun et al., 1998; Krizhevsky, 2009). The Variance Preserving (VP) process was used in all experiments with diffusion models, for which $b_+(\tilde{\mathbf{x}}_s, s) = -\beta(s)\tilde{\mathbf{x}}_s/2$ and $\sigma(s) = \sqrt{\beta(s)}$ in Eq. (2) (Sohl-Dickstein et al., 2015; Song et al., 2021b). The code is available on GitHub.

D.1 A JOINT GAUSSIAN MODEL

We revisit the linear model from Eq. (26), generalizing it to higher dimensional random variables $\mathbf{X} \in \mathbb{R}^{D_{\mathbf{X}}}$, $\mathbf{Y} \in \mathbb{R}^{D_{\mathbf{Y}}}$. That is,

$$\mathbf{Y} = A\mathbf{X} + \boldsymbol{\varepsilon}, \quad (54)$$

where $\mathbf{X} \sim \mathcal{N}(0, \Sigma_{\mathbf{X}})$ and $\boldsymbol{\varepsilon} \sim \mathcal{N}(0, \Sigma_{\boldsymbol{\varepsilon}})$. The joint vector $\mathbf{R} := (\mathbf{X}, \mathbf{Y})^{\top}$ is also Gaussian distributed, with zero mean, and covariance

$$\Sigma_{\mathbf{R}} = \begin{pmatrix} \Sigma_{\mathbf{X}} & \Sigma_{\mathbf{X}} A^{\top} \\ A \Sigma_{\mathbf{X}} & A \Sigma_{\mathbf{X}} A^{\top} + \Sigma_{\boldsymbol{\varepsilon}} \end{pmatrix} =: \begin{pmatrix} \Sigma_{\mathbf{X}} & \Sigma_{\mathbf{X}\mathbf{Y}} \\ \Sigma_{\mathbf{X}\mathbf{Y}} & \Sigma_{\mathbf{Y}} \end{pmatrix}. \quad (55)$$

This can be derived using $\Sigma_{\mathbf{X}\mathbf{Y}} \equiv \text{Cov}(\mathbf{X}, \mathbf{Y}) = \mathbb{E}[\mathbf{X}\mathbf{Y}^{\top}] - \mathbb{E}[\mathbf{X}]\mathbb{E}[\mathbf{Y}]^{\top}$ etc. The mutual information between \mathbf{X} and \mathbf{Y} is (cf. Eq. (29))

$$I(\mathbf{X}; \mathbf{Y}) = \frac{1}{2} \log \left(\frac{|\Sigma_{\mathbf{Y}}|}{|\Sigma_{\mathbf{Y}|\mathbf{X}}|} \right), \quad (56)$$

where $\Sigma_{\mathbf{Y}|\mathbf{X}} = \Sigma_{\boldsymbol{\varepsilon}}$ is just the average covariance of the distributions $\mathbf{Y}|\mathbf{X} \sim \mathbf{x} = \mathcal{N}(A\mathbf{x}, \Sigma_{\boldsymbol{\varepsilon}})$, and $\Sigma_{\mathbf{Y}}$ is defined in Eq. (55). In our experiments we set $A \sim \mathcal{N}(0, 1)^{D_{\mathbf{X}} \times D_{\mathbf{Y}}}$, $\Sigma_{\boldsymbol{\varepsilon}} = \sigma_{\boldsymbol{\varepsilon}}^2 I$, and

$$\Sigma_{\mathbf{X}} = HH^{\top} + \delta I, \quad (57)$$

where $H \sim \mathcal{N}(0, 1)^{D_{\mathbf{X}} \times D_{\mathbf{X}}} / \sqrt{D_{\mathbf{X}}}$ and $\delta > 0$ ensures numerical stability as well as positive definiteness of $\Sigma_{\mathbf{X}}$.

We can also compute the ideal score functions $\nabla \log p(\tilde{\mathbf{x}}_s, s|\mathbf{y})$ and $\nabla \log p(\tilde{\mathbf{x}}_s, s)$ under the forward process. The conditional density at time s are obtained by evolving the initial distribution of $\mathbf{X}|\mathbf{Y} \sim \mathbf{y}$, namely (see Bishop, 2006, Sec. 2.3.1)

$$\mathcal{N}(\Sigma_{\mathbf{X}\mathbf{Y}} \Sigma_{\mathbf{Y}}^{-1} \mathbf{y}, \Sigma_{\mathbf{X}} - \Sigma_{\mathbf{X}\mathbf{Y}} \Sigma_{\mathbf{Y}}^{-1} \Sigma_{\mathbf{X}\mathbf{Y}}) =: \mathcal{N}(\mu_{\mathbf{X}|\mathbf{Y}}, \Sigma_{\mathbf{X}|\mathbf{Y}}). \quad (58)$$

We use the VP process in our experiments, under which

$$\tilde{\mathbf{x}}_s = \sqrt{\alpha(s)}\mathbf{x} + \sqrt{1 - \alpha(s)}\boldsymbol{\eta}, \quad \boldsymbol{\eta} \sim \mathcal{N}(0, I). \quad (59)$$

Therefore, Eq. (58) is diffused to

$$p(\tilde{\mathbf{x}}_s, s | \mathbf{y}) = \mathcal{N}(\tilde{\mathbf{x}}_s; \mu_s^{\mathbf{X}|\mathbf{Y}}, \Sigma_s^{\mathbf{X}|\mathbf{Y}}), \quad (60)$$

$$\begin{aligned} \mu_s^{\mathbf{X}|\mathbf{Y}} &:= \mathbb{E}[\tilde{\mathbf{x}}_s | \mathbf{y}] = \sqrt{\alpha(s)} \Sigma_{\mathbf{X}|\mathbf{Y}} \Sigma_{\mathbf{Y}}^{-1} \mathbf{y} \equiv \sqrt{\alpha(s)} \mu_{\mathbf{X}|\mathbf{Y}}, \\ \Sigma_s^{\mathbf{X}|\mathbf{Y}} &:= \text{Cov}[\mathbf{X}_s | \mathbf{y}, \mathbf{X}_s | \mathbf{y}] \\ &= \mathbb{E}[(\mathbf{X}_s - \mu_s^{\mathbf{X}|\mathbf{Y}})(\mathbf{X}_s - \mu_s^{\mathbf{X}|\mathbf{Y}})^\top] \\ &= \alpha(s) \mathbb{E}[(\mathbf{X} - \mu_{\mathbf{X}|\mathbf{Y}})(\mathbf{X} - \mu_{\mathbf{X}|\mathbf{Y}})^\top] + (1 - \alpha(s)) I \\ &= \alpha(s) \Sigma_{\mathbf{X}|\mathbf{Y}} + (1 - \alpha(s)) I. \end{aligned}$$

Under Eq. (59), the marginal density at s is

$$p(\tilde{\mathbf{x}}_s, s) = \mathcal{N}(\tilde{\mathbf{x}}_s; 0, \Sigma_s^{\mathbf{X}}), \quad \Sigma_s^{\mathbf{X}} = \alpha(s) \Sigma_{\mathbf{X}} + (1 - \alpha(s)) I. \quad (61)$$

Similarly, if the joint distribution were evolved by a VP process acting on both components of \mathbf{R} , the density at an intermediate time is

$$p(\tilde{\mathbf{x}}_s, \tilde{\mathbf{y}}_s, s) =: p(\tilde{\mathbf{r}}_s, s) = \mathcal{N}(\tilde{\mathbf{r}}_s; 0, \Sigma_s), \quad \Sigma_s^{\mathbf{R}} = \alpha(s) \Sigma_{\mathbf{R}} + (1 - \alpha(s)) I. \quad (62)$$

Then, the conditional, marginal, and joint scores are

$$\nabla_{\tilde{\mathbf{x}}_s} \log p(\tilde{\mathbf{x}}_s, s | \mathbf{y}) = - \left(\Sigma_s^{\mathbf{X}|\mathbf{Y}} \right)^{-1} \left(\tilde{\mathbf{x}}_s - \mu_s^{\mathbf{X}|\mathbf{Y}} \right), \quad (63a)$$

$$\nabla_{\tilde{\mathbf{x}}_s} \log p(\tilde{\mathbf{x}}_s, s) = - \left(\Sigma_s^{\mathbf{X}} \right)^{-1} \tilde{\mathbf{x}}_s, \quad (63b)$$

$$\nabla_{\tilde{\mathbf{r}}_s} \log p(\tilde{\mathbf{r}}_s, s) = - \left(\Sigma_s^{\mathbf{R}} \right)^{-1} \tilde{\mathbf{r}}_s. \quad (63c)$$

Equipped with these formulas we can verify points 1 to 3 while sidestepping the singular behavior of neural entropy in image diffusion models. For each experiment with the joint Gaussian, a conditional diffusion model is trained on $\{(\mathbf{x}^{(i)}, \mathbf{y}^{(i)})\}_{i=1}^N$, and a second model learns the marginal of \mathbf{X} from $\{(\mathbf{x}^{(i)})\}_{i=1}^N$ alone. These models use a simple MLP core, and we train with the maximum likelihood denoising objective (Eq. (47) with $\lambda(s) = \sigma(s)^2/2$). The experiments are described below.

Entropy and correlation We train on samples of Eq. (54) for $D_{\mathbf{X}} = 25$, $D_{\mathbf{Y}} = 15$, with A kept fixed and $\sigma_\epsilon = 1.0, 0.6, 0.25$. Reducing the noise strength increases $I(\mathbf{X}; \mathbf{Y})$ (cf. Fig. 2), as well as the conditional neural entropy $S_{\text{NN}}^{\mathbf{X}|\mathbf{Y}}$. We also plot the true value of these quantities calculated with the analytic scores in Eq. (63c). The resulting entropy curves are shown in Fig. 5. Notice how the peak of the entropy rate curves becomes more localized at earlier s as the correlation between \mathbf{X} and \mathbf{Y} is made stronger. This is the same effect that gives rise to the sharp peak in the neural entropy rates for image diffusion models (see Fig. 8).

Mutual information and guidance In Sec. 4, we explained how CFG increases $I(\mathbf{X}; \mathbf{Y})$. For the joint Gaussian \mathbf{Y} is not a discrete random variable like a class label. Nonetheless, we can study how a ‘CFG-style’ modification to the reverse drift affects the samples from Eq. (54). Since we know the true scores, we can produce samples with the probability flow ODE (Maoutsou et al., 2020),

$$d\mathbf{x}_t = \left(-b_+(\mathbf{x}_t, T - t) + \frac{\sigma(T - t)^2}{2} [(1 + w) \nabla \log p(\mathbf{x}_t, t | \mathbf{y}) - w \nabla \log p(\mathbf{x}_t, t)] \right) dt. \quad (64)$$

A simple example of the samples generated by Eq. (64) is shown in Fig. 1. CFG tightens the dependence of \mathbf{X} on \mathbf{Y} , but also skews the true relationship between them (see Sec. C.2). Going to higher dimensions, we set $D_{\mathbf{X}} = 25$ and generate training data with Eq. (64) for $D_{\mathbf{Y}} = 5, 10, 25$, with a range of CFG weights $w \in (0, 6)$. We train a pair of diffusion models to reconstruct $\mathbf{X}|\mathbf{Y}$ and \mathbf{X} , and estimate $I(\mathbf{X}; \mathbf{Y})$ using the MINDE formula, Eq. (14). The results are plotted in Fig. 4.

As expected, CFG does increase the mutual information between \mathbf{X} and \mathbf{Y} . Two observations stand out: first, the increase in $I(\mathbf{X}; \mathbf{Y})$ saturates at larger w , and second, the gain in $I(\mathbf{X}; \mathbf{Y})$ is higher at larger $D_{\mathbf{Y}}$. Both these features can be understood through the information bottleneck principle from Sec. A.2: the degree to which the binding between \mathbf{X} and \mathbf{Y} can be strengthened is limited by the number of degrees of freedom in \mathbf{Y} .

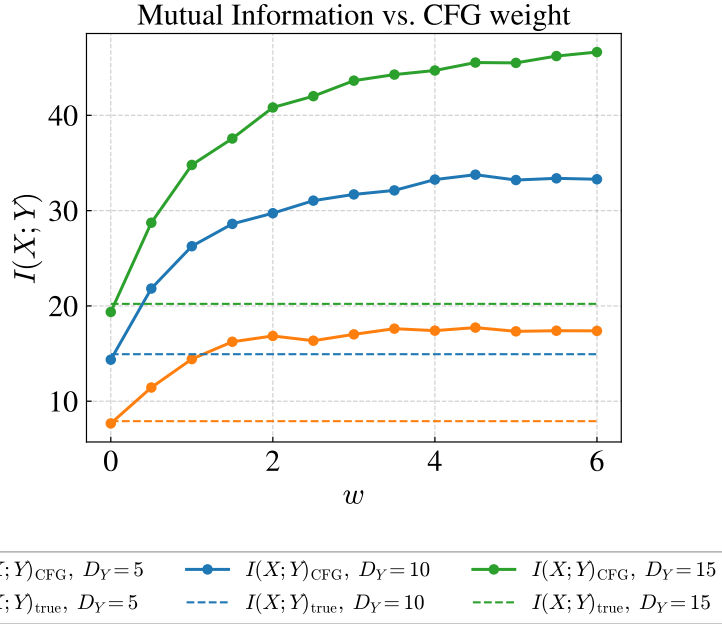


Figure 4: Mutual information under CFG for the joint Gaussian model from Eq. (54). We fix $D_{\mathbf{X}} = 25$ and repeat the experiment with $D_{\mathbf{Y}} = 5, 10, 15$. Notice how $I(\mathbf{X}; \mathbf{Y})_{\text{CFG}}$ increases as the guidance strength is ramped up. It saturates faster for smaller $D_{\mathbf{Y}}$, when \mathbf{Y} has fewer degrees of freedom to encode the diversity in \mathbf{X} . This is also why the mutual information between images and labels is low in the first place. $I(\mathbf{X}; \mathbf{Y})_{\text{CFG}}$ was estimated using Eq. (14), with diffusion models trained on data generated with CFG. The true value of mutual information is known from Eq. (56).

E INFORMATION HIERARCHY

E.1 VAE vs. DAE

In Sec. 5 we discussed diffusion autoencoders and pointed out that they help understand how the diffusion models store information. To see how this works, we start by comparing the diffusion model in the DAE with a simpler Gaussian-likelihood decoder, $p_{\psi}(\mathbf{x}|\mathbf{z}) = \mathcal{N}(\mathbf{x}; f_{\psi}(\mathbf{z}), \sigma_{\text{dec}}^2 I)$, where σ_{dec} is a constant and ψ are the network parameters. Minimizing the ℓ_2 loss of this decoder,

$$\mathbb{E}_{q_{\phi}(\mathbf{z}|\mathbf{x})}[-\log p_{\psi}(\mathbf{x}|\mathbf{z})] \propto \mathbb{E}_{\mathbf{z} \sim q_{\phi}(\cdot|\mathbf{x})}[\|\mathbf{x} - f_{\psi}(\mathbf{z})\|^2], \quad (65)$$

is equivalent to predicting the the conditional mean $\mathbb{E}[\mathbf{x}|\mathbf{z}]$, which lies between the modes of the true distribution (Bishop, 2006). As a result, in image processing applications, the reconstructions from such a decoder tend to be blurry (Wang & Bovik, 2009). On the other hand, the diffusion decoder from Eq. (18) generates a new sample by progressively evolving a random vector toward a denoised mean that becomes more resolved over time (see Sec. 6 and Fig. 13). Therefore, these models can capture the multi-modal structure of the underlying distribution with greater fidelity, producing reconstructions that are far more faithful to the original signal (see Fig. 6). Since the diffusion decoder retains more information about each \mathbf{x} , it can distinguish samples with greater accuracy. This places a greater strain on the encoder as it is pressured to supply more differentiated latent codes to disambiguate the richer variety of data points.

The latents in an autoencoder serve as a probe of the decoder’s ability to capture information. This is borne out in a simple experiment comparing the latents from a DAE to those from a VAE with the Gaussian decoder in Eq. (65), both of which use the same encoder architecture. We train both autoencoders to reconstruct MNIST images, restricting ourselves to latent dimensions of $D_{\mathbf{Z}} = 2$ for easier visualization of the aggregated posterior, $q_{\phi}(\mathbf{z}) = \sum_{\mathbf{x}} q_{\phi}(\mathbf{z}|\mathbf{x})p_{\text{d}}(\mathbf{x})$. Even at this low $D_{\mathbf{Z}}$ we observe discernible clustering in the VAE latent, corresponding to the different digits. By contrast, in the latent space of the DAE the clusters are more blended, with weaker separation between digit classes (see Fig. 7). The suggests that the DAE perceives greater similarity between

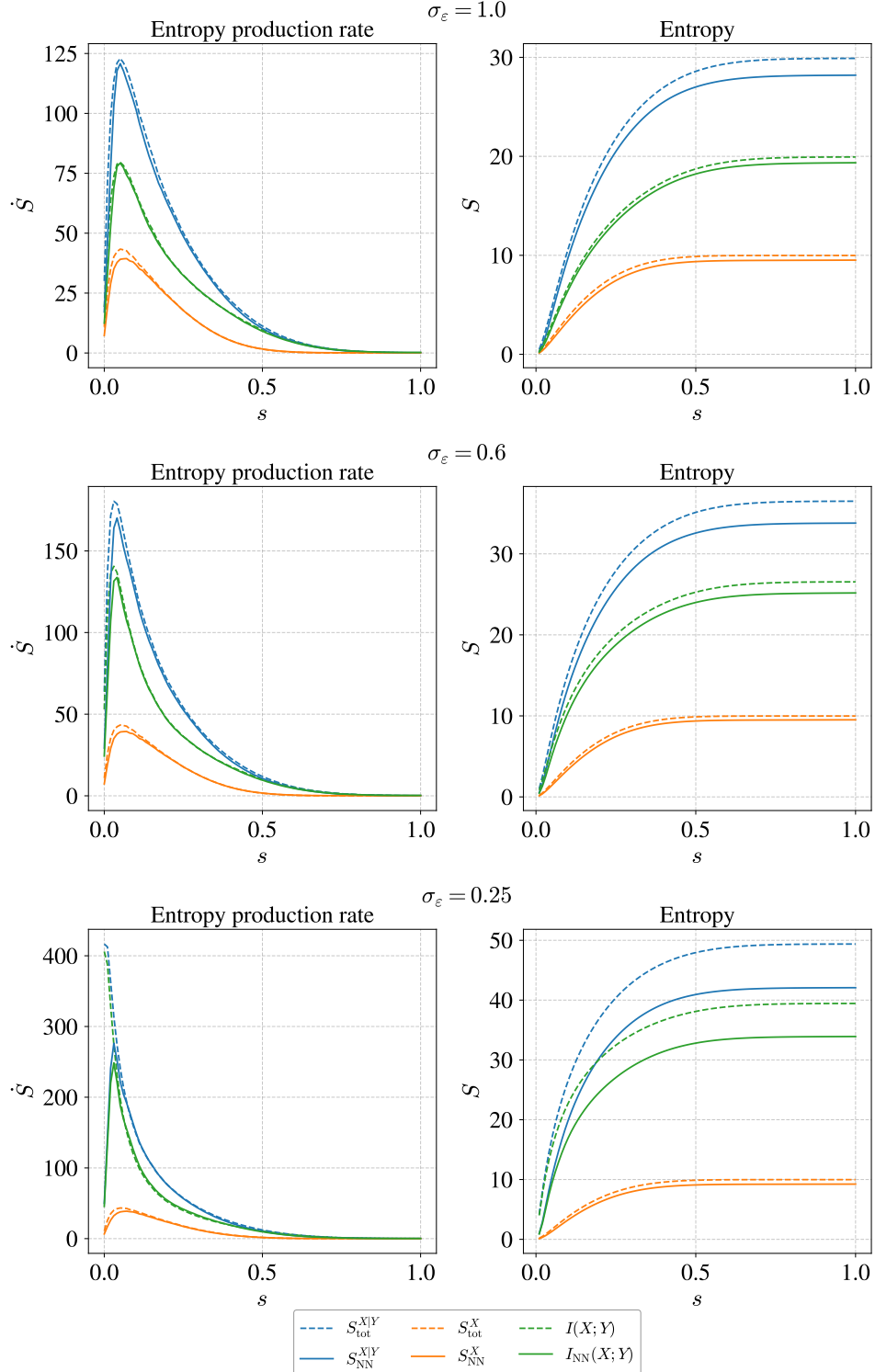


Figure 5: Evolution of total entropy, neural entropy, and the mutual information under the forward process, for a joint Gaussian with $D_X = 25$, $D_Y = 15$. As σ_ε is lowered \mathbf{X} and \mathbf{Y} become more correlated, which causes the mutual information and the neural entropies to grow. Notice also how the entropy rate curves become more concentrated near $s = 0$; as $\sigma_\varepsilon \rightarrow 0$, \mathbf{X} and \mathbf{Y} converge on the hyperplane $\mathbf{Y} = A\mathbf{X}$ which takes an infinite amount of information to locate precisely (see Fig. 3). Diffusion models struggle to keep pace with the informational load as we approach this limit.

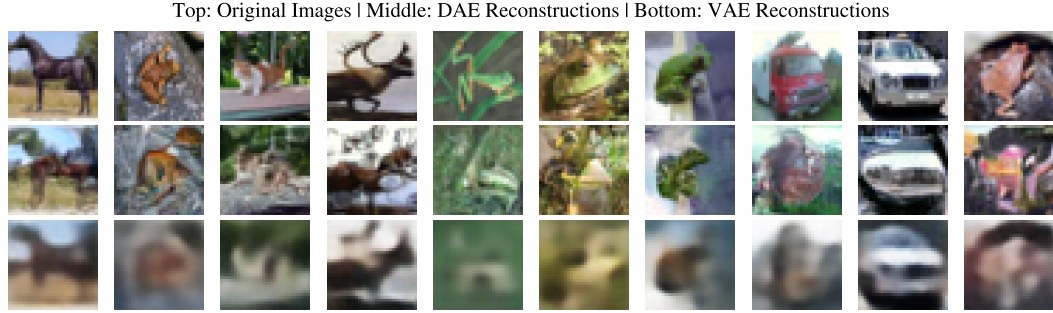


Figure 6: Images reconstructed by a DAE and VAE. Both of them have the same encoder architecture. The VAE uses a Gaussian decoder that tends to produce blurrier outputs, whereas the diffusion decoder captures significantly more textural detail, leading to sharper images. In this example, the convolutional encoder’s simplicity limits the fidelity of the DAE reconstruction.

MNIST latents with $D_Z = 2$

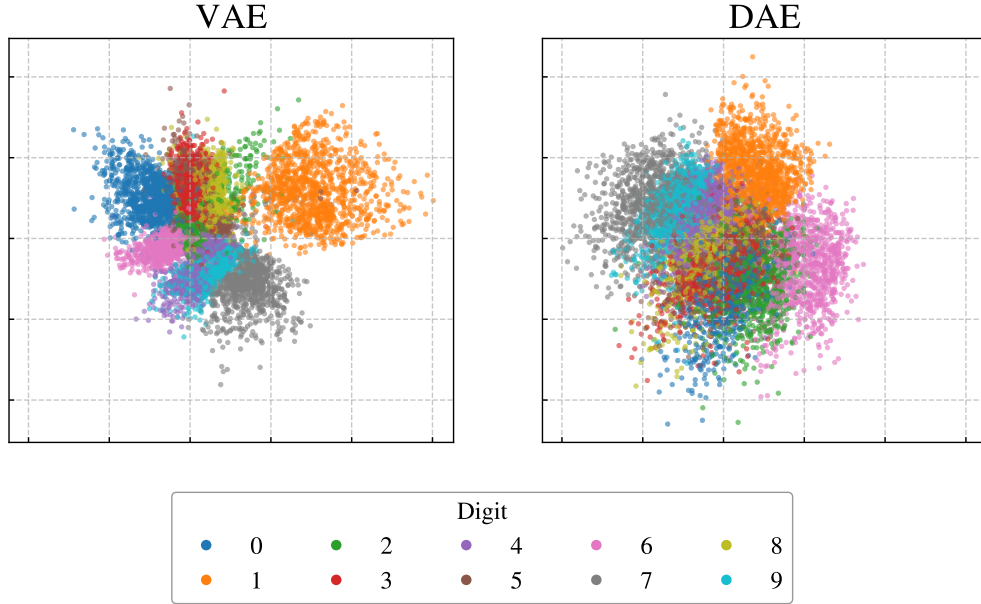


Figure 7: Latents from a VAE and DAE trained to reconstruct MNIST digits. Distinct clusters appear in the VAE latent, even at the low dimensionality of $D_Z = 2$. On the other hand, the DAE’s latent clusters are more blended, because the small-scale details captured by the diffusion decoder are similar for all digits, and this information overwhelms the semantic differences. See also Fig. 9a.

different digits than the VAE, the common information across digit classes being the high-frequency detail washed away by the averaging effect of the Gaussian decoder. If we widen the bottleneck by increasing D_Z , we find better separation between the DAE clusters, since there is more room to encode the rich detail preserved by the diffusion decoder.

The above experiment gives us a clue as to why image diffusion models often neglect conditioning on class labels. The *semantic* information that identifies the digit ‘1’ from an image of ‘1’ is a relatively small fraction of the total information content in that image. The rest encodes *perceptual* details that have a similar distribution for all images, even those of different digits. Therefore, the marginal \mathbf{X} and the conditional $\mathbf{X} | \mathbf{Y} = \mathbf{y}$ possess comparable entropy—specifying the class label does not reduce the uncertainty in \mathbf{X} by a lot. In other words, the mutual information between these images and their labels is low; the problem lies in the data itself. CFG is a trick to boost $I(\mathbf{X}; \mathbf{Y})$

post-training, but it merely amplifies whatever signal is already present; *multiplying a weak signal also magnifies the noise*.

E.2 SEMANTIC VS. PERCEPTUAL

Why must the diffusion model devote a large fraction of its information budget to resolving the microscopic details of the image? And how do we know it is these details that overwhelm the semantic information? To answer these questions, we begin by noting that forward diffusion dissolves the perceptual details in the first few steps, whereas the semantic structure is preserved—we can still read off a digit from a noisy image of it. More prosaically, natural images follow a power-law spectrum, which means the low frequencies dominate while high frequency (short wavelength) modes are subdued (Ruderman, 1994). Since the white noise term in Eq. (2) injects equal power across all frequencies, the finer details fade away more rapidly when images are diffused. Therefore, we expect entropy production associated with the removal of perceptual detail to be localized in a narrow interval near $s = 0$. The neural entropy rates in Fig. 8 exhibit a sharp peak in this range, which answers the second question.

We can also understand Fig. 8 from a geometric perspective by viewing S_{NN} as the information the network injects in the t -direction. The data distribution resides on a low-dimensional submanifold of the ambient pixel space. The reduced dimensionality of the data manifold stems from the fact that nearby pixels are very strongly correlated in high-fidelity images, so there are fewer degrees of freedom than the naive pixel count. In the generative stage, the diffusion model drives a high-dimensional Gaussian distribution back onto the lower-dimensional data manifold (see Fig. 3). The sharp rise in entropy rate as $t \rightarrow T$ is reflective of the fact that the network must supply substantial information to locate the manifold exactly, which involves collapsing the distribution to delta functions along all directions orthogonal to its tangent space. This singular behavior can also be traced back to the total correlation term in Eq. (11), as explained in Sec. 4, and at the end of Sec. A.1. This addresses the first question.

In Sec. 6 we conceptualized a diffusion model as an infinite tower of autoencoders, one for each instant s in the forward diffusion process. The encoder was denoted by the operator \mathcal{D}_s and the decoder by \mathcal{D}_s^\dagger . The shallow/small- s autoencoders are responsible for the small-scale details, whereas the deeper ones attend to the macroscopic features. It is possible to peer into this tower using a DAE, by conditioning its diffusion model on separate latents over different intervals in s . Recall Eq. (18), which we shall write as

$$\mathbb{E}_{\mathbf{X}, \mathbf{Z}}[-\log p_{\boldsymbol{\theta}}(\mathbf{x}|\mathbf{z})] + c(T) \leq \int_0^T ds \mathbb{E}_{\mathbf{Z}}[L(\mathbf{z}; s)], \quad (66)$$

$$L(\mathbf{z}; s) := \mathbb{E}_{\mathbf{X}, \tilde{\mathbf{X}}_s} \left[\frac{\sigma^2}{2} \left\| \nabla \log p_{\text{eq}}^{(s)}(\tilde{\mathbf{x}}_s) - \nabla \log p(\tilde{\mathbf{x}}_s, s|\mathbf{x}, 0) + \mathbf{e}_{\boldsymbol{\theta}}(\tilde{\mathbf{x}}_s, s; \mathbf{z}) \right\|^2 \right]. \quad (67)$$

Notice that if the integrate L from an intermediate time $s = \tau$ up to T the l.h.s. must be updated with the reconstructed density at τ ,

$$\mathbb{E}_{\tilde{\mathbf{X}}_\tau, \mathbf{Z}_{\text{sem}}}[-\log p_{\boldsymbol{\theta}}(\tilde{\mathbf{x}}_\tau, \tau|\mathbf{z}_{\text{sem}})] + c(\tau) \leq \int_\tau^T ds \mathbb{E}_{\mathbf{Z}}[L(\mathbf{z}_{\text{sem}}; s)], \quad (68)$$

where $c(\tau)$ is still independent of $\boldsymbol{\theta}$. The latent \mathbf{z}_{sem} encodes $\tilde{\mathbf{X}}_\tau$, the version of \mathbf{X} that has been forward diffused for a time τ . In other words, \mathbf{z}_{sem} represents the information stored in the $\mathcal{D}_s/\mathcal{D}_s^\dagger$ autoencoders for $s \geq \tau$. Following our earlier logic, \mathbf{z}_{sem} manages to evade much of the perceptual information—it ‘sees’ images where most of these microscopic details have been washed out and only the semantic structure remains—if τ is chosen judiciously. We can introduce another latent, \mathbf{z}_{per} , to aggregate the information from the $(0, \tau)$. Therefore, Eq. (66) can be split into

$$\begin{aligned} & \mathbb{E}_{\mathbf{X}, \mathbf{Z}_{\text{sem}}, \mathbf{Z}_{\text{per}}}[-\log p_{\boldsymbol{\theta}}(\mathbf{x}|\{\mathbf{z}_{\text{sem}}, \mathbf{z}_{\text{per}}\})] + c(T) \\ & \leq \int_0^\tau ds \mathbb{E}_{\mathbf{Z}_{\text{per}}}[L(\mathbf{z}_{\text{per}}; s)] + \int_\tau^T ds \mathbb{E}_{\mathbf{Z}_{\text{sem}}}[L(\mathbf{z}_{\text{sem}}; s)]. \end{aligned} \quad (69)$$

Thus, \mathbf{Z}_{sem} and \mathbf{Z}_{per} access information from different epochs of the forward diffusion process. We can verify points 4 and 5 by examining each of these latents closely.

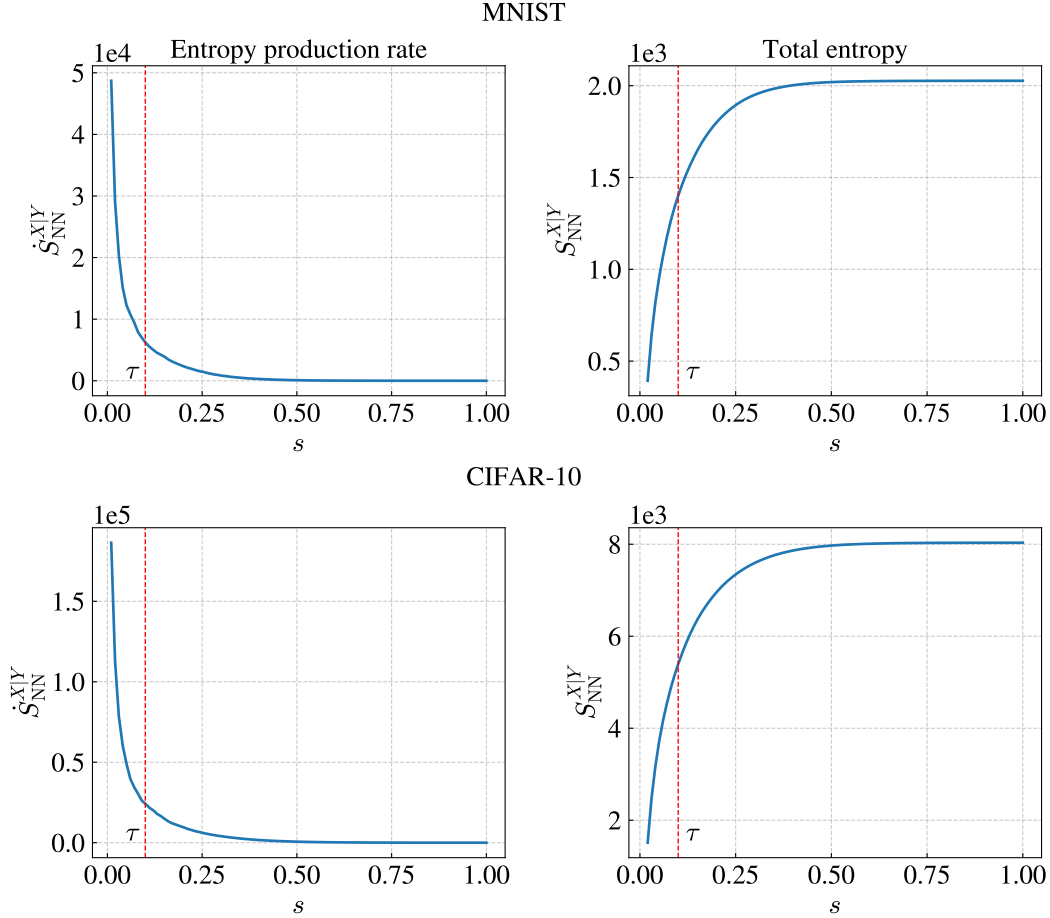
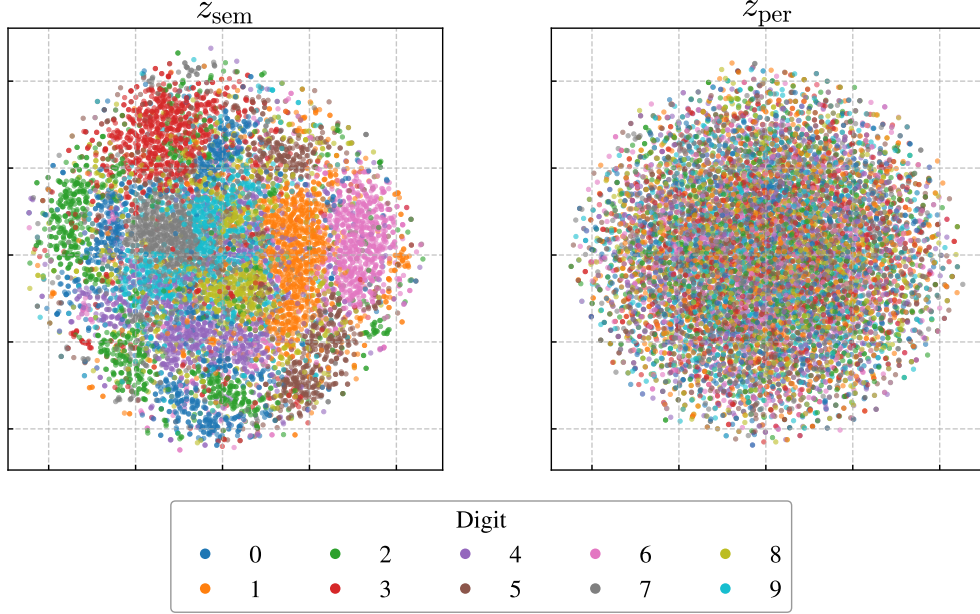


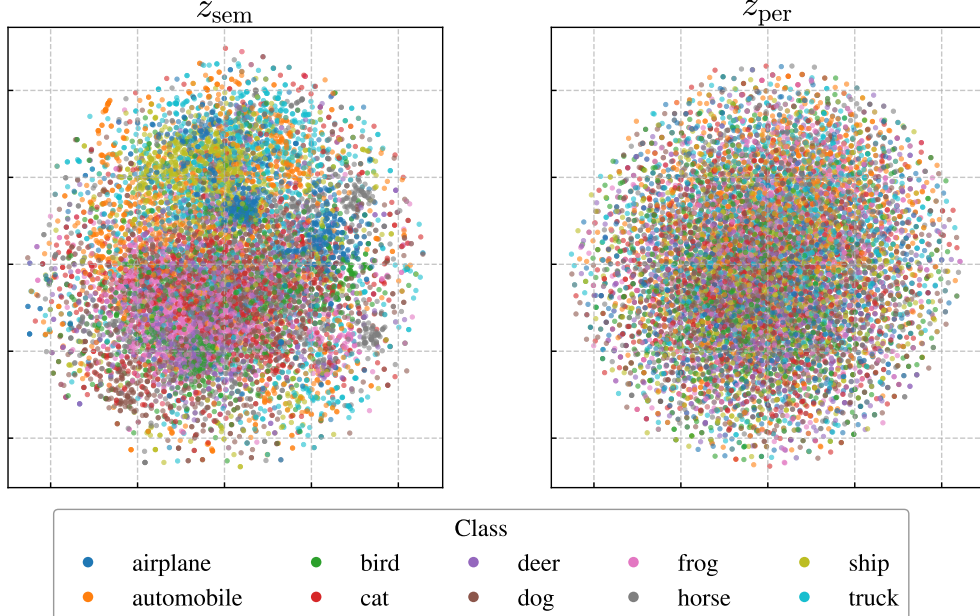
Figure 8: Neural entropy profiles for two image diffusion models trained on the MNIST and CIFAR-10 datasets. On the left is the entropy production rate, which is the time derivative of the neural entropy $S_{\text{NN}}^{X|Y}$, defined in Eq. (12). Its value at s is the information stored in the autoencoder at depth s in the infinite tower (cf. Sec. 6). The sharp rise in entropy rate at early s is attributed to the low dimensionality of the data manifold. The same effect can be observed in a simple Gaussian model if the correlation between variables becomes too strong Fig. 5. It should be stressed that the singular behavior of $\dot{S}_{\text{NN}}^{X|Y}$ is different from the numerical divergence at $s = 0$ due to the vanishing of $\Sigma(s)$ in Eq. (43). The dashed red line indicates the partitioning of the denoising loss into semantic and perceptual pieces for the experiments in Sec. E.2.

2D t-SNE plot of MNIST latents



(a) A 2D t-SNE plot of the 20-dimensional latents z_{sem} and z_{per} produced by a DAE trained on MNIST digits. Information erased by the forward process up to $\tau = 0.1T$ is encoded in perceptual latent z_{per} , whereas all information beyond this point is captured by the semantic latent z_{sem} . Clusters of z_{sem} correspond to different MNIST digits. On the other hand, z_{per} shows little structure because the textural details of the images are very evenly distributed amongst all the digit classes.

2D t-SNE plot of CIFAR-10 latents



(b) t-SNE for CIFAR-10 latents. The more nuanced structure of z_{sem} reflects the far higher semantic variation between images in CIFAR-10. Both z_{sem} and z_{per} had $D_Z = 60$ dimensions.

Figure 9

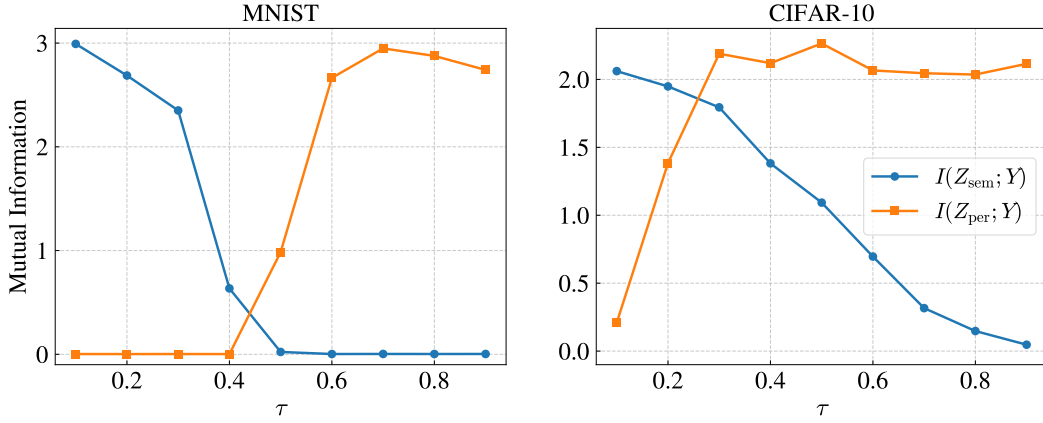


Figure 10: Mutual information between the image labels Y and the corresponding semantic and perceptual latents, as a function of the partitioning time τ (cf. Eq. (69)). At early τ the semantic latent is strongly correlated with the labels, whereas the perceptual details are completely independent. As τ increases Z_{sem} becomes progressively irrelevant, whereas Z_{per} does the opposite—knowing enough small-to-medium details helps the model understand what the image is.

We begin by visualizing Z_{sem} and Z_{per} for DAE’s trained on MNIST and CIFAR-10 (see Fig. 9). We use $D_Z = 20$ for the former and $D_Z = 60$ for the latter, for both semantic and perceptual latents. These are generated by separate convolutional encoders. Optionally, we can adjust the receptive field of Z_{sem} to be larger than that of Z_{per} by increasing the number of encoder layers, as we do. These are mapped to two-dimensional space using t-SNE (van der Maaten & Hinton, 2008). With $\tau = 0.1T$, we find that there is little to no structure in Z_{per} in either case, in agreement with our claim that images from different classes have similar small-scale details. On the other hand, clusters of Z_{sem} appear in the t-SNE plot, showing that class labels correspond to large-scale features robust to small perturbations.⁵

We can do better than inspect Z_{sem} and Z_{per} by eye. Recall that Eq. (13) can be used to estimate the mutual information between random variables. By training a small diffusion model on pairs $\{(z_i, y)\}_{i=1}^N$, we can find the determine $I(Z_{\bullet}, Y)$ approximately. The results are plotted in Fig. 10 for a range of τ values. As expected, Z_{sem} correlates well with Y at small τ , whereas Z_{per} is nearly independent of it. However, as τ is increased Z_{per} rapidly encodes class information. We speculate that the $X \rightarrow Z_{\text{per}}$ encoder can detect semantic meaning if it’s given sufficient information about the medium-scale features, since an image is the sum of its parts. Furthermore, if τ is not too close to $s = 0$, the encoder focuses effort on information that differentiates the images, and downplays the shared textural detail between them. This is why Fig. 7 showed *some* clustering in the DAE case—even with the large amount of small-scale information the diffusion decoder captures, the encoder is incentivized to construct latents that uniquely identify the images (cf. Sec. 5). We also mention in passing that the cross-over phenomenon in Fig. 7 is reminiscent of the *critical windows* of feature emergence (Li & Chen, 2024).

F NOTATION

The natural logarithm is denoted by \log . In Sec. 2 we use the symbol H for Shannon entropy of a discrete random variable, and $I(X, Y)$ is in bits. Everywhere else we use the differential entropy $S := -\int p \log p$, and the mutual information is in nats. Scalars are written in plain letters, while boldface symbols such as X, Y, Z denote higher-dimensional random variables. We write x for a realization of X , with unsubscripted symbols always referring to the data distribution p_d . We also write $p_d(x, y)$ for the joint data distribution.

⁵This is why the diffusion classifiers from Clark & Jaini (2023); Li et al. (2023) employ a denoising objective that significantly downweights the contributions from the earlier time steps. The popular practice of ‘variance-dropping’ also achieves a similar effect (see Sec. B.3).

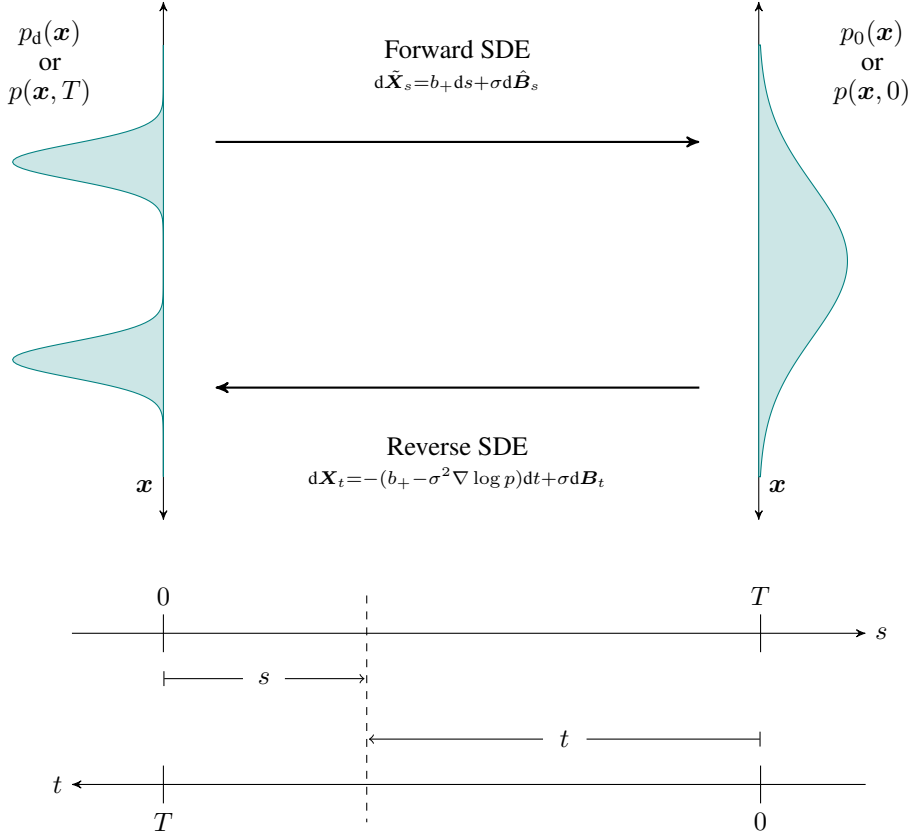


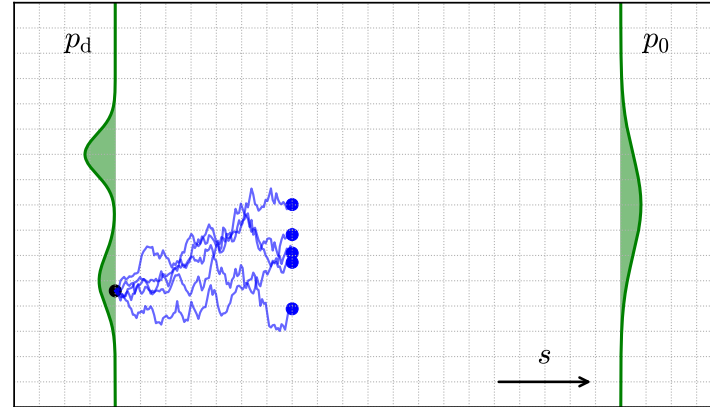
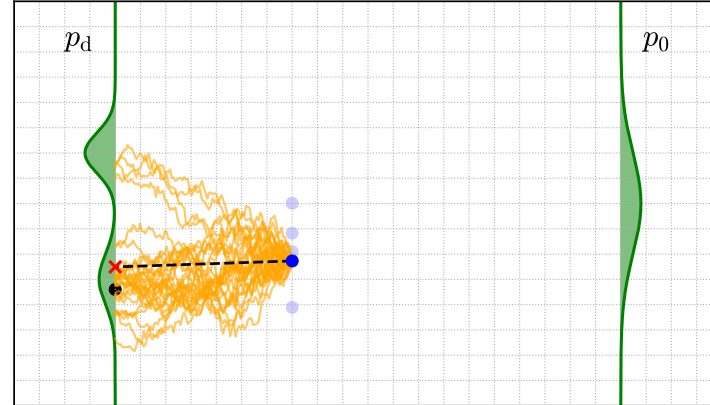
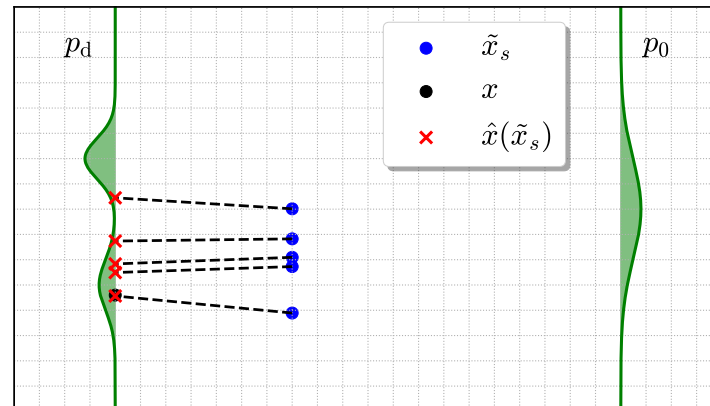
Figure 11: A schematic of the forward and reverse diffusion processes.

We use the time variable s for the forward diffusion process, which runs from left ($s = 0$) to right ($s = T$) in Fig. 11. $\hat{\mathbf{B}}_s$ and \mathbf{B}_t denote the Brownian motions associated with the forward and reverse/controlled SDEs, respectively. ∇ is the gradient with respect the spatial coordinates, and ∂_t, ∂_s are partial time derivatives. S_{tot} is the total entropy produced during forward diffusion, and is closely approximated by the neural entropy S_{NN} . The time-dependence of the entropies is implicit in most of the main text; S_{tot} and S_{NN} without the time argument should be understood as $S_{\text{tot}}(s = T) \equiv S_{\text{tot}}(T)$.

The density $p(\tilde{\mathbf{x}}_s, s)$ is the same as $p(\mathbf{x}_t, t)$. That is, the symbol p is overloaded so we do not have to write $p(\cdot, s) = p(\cdot, T - t)$ everywhere. Throughout the paper, we set Boltzmann's constant to unity, $k_B = 1$. p_d and p_0 denote the initial ($s = 0$) and final ($s = T$) densities for the forward process, and p_{eq} is its equilibrium state. Diffusion takes an infinite time to equilibrate, but we always take T to be large compared to the intrinsic time scale of the diffusion process.

G ILLUSTRATIONS

This section contains illustrations related to the discussion in Sec. 6.

(a) Forward diffusion from a test point x produces noisy samples \tilde{x}_s .(b) $\hat{x}(\tilde{x}_s)$ is the average of all landings at $s = 0$ of reverse trajectories that start at \tilde{x}_s .(c) Each \tilde{x}_s maps back to its own denoised mean $\hat{x}(\tilde{x}_s)$.Figure 12: A breakdown of how $-\log p_d(x)$ is computed in Eq. (23). The denoised means $\hat{x}(\tilde{x}_s)$ from many \tilde{x}_s give a sense of the regions in p_d that are most like x .

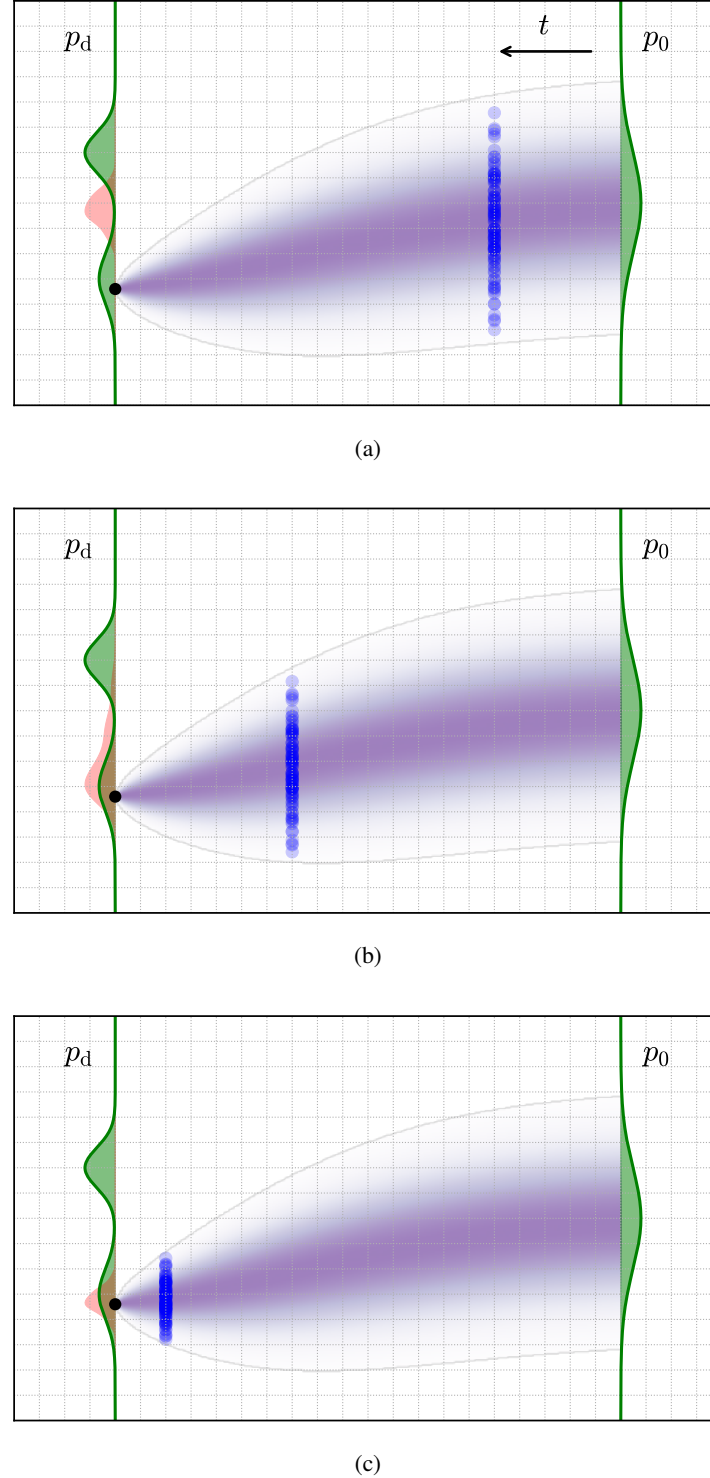


Figure 13: Iterative resolution of a sample from p_d . The red curve shows the density of denoised means computed from the blue points using the Miyasawa relation, Eq. (44). As we progress along the t -direction, the dynamics steers us toward the denoised mean, making the band of blue points narrower, which produces a sharper estimate of the denoised mean, gradually refining the sample toward its limiting value.